Chemical Science

ROYAL SOCIETY OF CHEMISTRY

REVIEW

View Article Online
View Journal | View Issue

Cite this: *Chem. Sci.*, 2025, **16**, 8217

Critical issues and optimization strategies of vanadium dioxide-based cathodes towards high-performance aqueous Zn-ion batteries

Botao Wan,†[a] Yajiang Wang,†[a] Xiudong Chen,*[a] Changchao Zhan,[a] Huixiong Jiang,[a] Jin-Hang Liu,[a] Yun Gao,*[bc] Xiaoduo Jiang,[a] Xiaohua Cao,[a] Hang Zhang,*[bcd] Shi-Xue Dou[e] and Yao Xiao*[bcd]

Aqueous zinc-ion batteries (AZIBs) are gaining significant attention due to their excellent safety, cost-effectiveness, and environmental friendliness, making them highly competitive energy storage solutions. Despite these advantages, the commercial application of AZIBs faces substantial challenges, particularly those related to performance limitations of cathode materials. Among potential candidates, vanadium dioxide (VO_2) stands out due to its exceptional electrochemical properties and unique crystal structure, rendering it a promising cathode material for AZIB applications. The review summarizes the recent research progress on VO_2 in AZIBs, analyzes its crystal structures (tetragonal VO_2(A), monoclinic VO_2(B, D, M), and rutile VO_2(R)), morphology and energy storage mechanisms (Zn^{2+} insertion/extraction, H^+/Zn^{2+} co-insertion/extraction, and chemical reaction mechanism), and discusses the relationship between the structure and performance. The review also addresses key challenges associated with VO_2 as a cathode material, including dissolution, by-product formation, and limited ion diffusion kinetics. To overcome these issues, various optimization strategies are systematically discussed, such as ion/molecule pre-intercalation, composite material fabrication, defect engineering, and elemental doping. Finally, potential research directions and strategies to further enhance the performance and commercial viability of VO_2-based cathodes are proposed.

Received 10th March 2025
Accepted 14th April 2025

DOI: 10.1039/d5sc01889g

rsc.li/chemical-science

1. Introduction

The international community has increasingly prioritized addressing global climate change, establishing carbon neutrality as a shared objective.[1,2] Energy storage systems are essential for advancing energy transformation and supporting low-carbon development, particularly in response to the ongoing growth in global energy demand.[3–6] High-performance energy storage systems play a crucial role in reducing reliance on fossil fuels, optimizing and upgrading the energy infrastructure, and promoting sustainable energy utilization. Additionally, they facilitate efficient energy allocation, providing robust technical support to ensure the achievement of carbon neutrality.[7–9] Lithium-ion batteries (LIBs) are widely recognized as one of the most advanced energy storage technologies available today, valued for their unique advantages.[10–13] LIBs offer a long cycle life with minimal capacity decay, ensuring durability over extended periods of working. Additionally, their low self-discharge rate minimizes energy loss during periods of inactivity. These characteristics have led to their widespread adoption in electric vehicles, portable electronic devices, and large-scale energy storage systems.[14–22] However, LIBs are prone to overheating during charging and discharging, with a potential risk of thermal runaway and organic electrolyte combustion. Furthermore, the large-scale application of LIBs is heavily influenced by the limited availability of lithium metal, which is affected by geopolitical factors, resource distribution, and other constraints.[23] Addressing these issues requires the development of energy storage devices that combine high capacity, environmental sustainability, and superior safety.[24–26]

Aqueous rechargeable metal-ion batteries, such as those based on potassium,[27] sodium,[28] magnesium,[29] aluminum,[30] and zinc, have garnered significant attention due to their high capacity, safety, and environmental sustainability. Among

[a]*School of Chemistry and Chemical Engineering, Jiangxi Province Engineering Research Center of Ecological Chemical Industry, Jiujiang University, Jiujiang 332005, China. E-mail: chenxd@jju.edu.cn*

[b]*College of Chemistry and Materials Engineering, Wenzhou University, Wenzhou, Zhejiang 325035, China. E-mail: yungao1995@shu.edu.cn; hang@wzu.edu.cn; xiaoyao@wzu.edu.cn*

[c]*Wenzhou Key Laboratory of Sodium-Ion Batteries, Wenzhou University Technology Innovation Institute for Carbon Neutralization, Wenzhou, Zhejiang 325035, China*

[d]*Key Laboratory of Advanced Energy Materials Chemistry (Ministry of Education), College of Chemistry, Nankai University, Tianjin 300071, China*

[e]*Institute of Energy Materials Science (IEMS), University of Shanghai for Science and Technology, Shanghai 200093, China*

† Botao Wan and Yajiang Wang contributed equally to this work.

these, aqueous zinc-ion batteries (AZIBs) stand out as a particularly promising contender.[31,32] AZIBs offer several advantages, including a high theoretical specific capacity of 800 mA h g^{-1}, a low redox potential of −0.76 V, and abundant natural zinc reserves.[33–36] To fully exploit these benefits, the development of cathode materials plays a pivotal role in determining the performance of rechargeable batteries. For the commercialization of AZIBs, structurally stable and high-capacity cathode materials are essential.[32,37,38] The cathode materials for AZIBs can be broadly categorized into manganese (Mn)-based materials,[39,40] vanadium-based materials,[41] Prussian blue analogs (PBAs),[42] organic compounds,[37] and other types.[43,44] Manganese-based compounds offer notable advantages, such as resource abundance and low cost, making them attractive options for AZIB cathodes. However, their practical development is hindered by challenges such as poor electrical conductivity and high solubility, which significantly impact their performance and stability.[35] PBAs are distinguished by their open three-dimensional framework and high working voltage. Nevertheless, their application is limited by structural instability, which can lead to structural collapse, capacity fading, and performance degradation during cycling. Similarly, the development of organic compounds as cathode materials faces challenges due to their complex synthesis processes and susceptibility to side reactions, which further hinder their practical implementation.[45] Vanadium-based compounds are considered promising candidates for next-generation AZIB cathodes due to their open framework structures, low cost, and high specific capacity.[46] Among these, vanadium dioxide (VO_2) stands out due to its unique crystal structure and high reversible specific capacity. Additionally, the stable structure and excellent ion transport properties of VO_2 provide superior performance and enhanced safety compared to other vanadium oxides, making it an especially attractive option for AZIB applications.[47]

VO_2, with its unique physicochemical properties, has been extensively studied as a cathode material for AZIBs, demonstrating significant potential for practical applications. However, comprehensive and systematic analyses of its progress, challenges, and commercial prospects remain limited. This review focuses on the structure–activity relationship between the VO_2 crystal structure and zinc storage performance, delves into its energy storage mechanisms, and underscores its critical role in energy conversion and storage (Fig. 1). Despite its strengths, VO_2 faces challenges akin to those of other metal oxide cathode materials, including poor structural stability, reduced cycling performance, and the loss of active sites, which collectively constrain its wider application in AZIBs. To overcome these obstacles, researchers have proposed several innovative approaches to stabilize the VO_2 crystal structure and enhance its electrochemical performance. Ion intercalation, for instance, achieves simultaneous improvements in structural stability and ion conductivity through precise control of the VO_2 lattice structure. Molecular intercalation exploits interactions between organic or other molecules and VO_2 layers to effectively enhance the material's electrochemical properties. The composite material strategy integrates VO_2 with other functional materials, leveraging synergistic effects to substantially

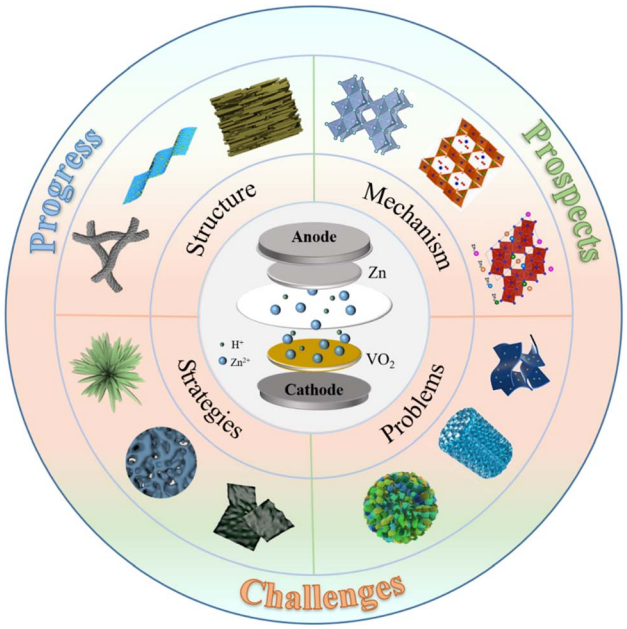

Fig. 1 Schematic illustration showing the recent advances in VO_2-based cathode materials for AZIBs.[61] Copyright 2021, Wiley-VCH.[69] Copyright 2019, American Chemical Society.[74] Copyright 2021, Elsevier.[76] Copyright 2023, Elsevier.[104] Copyright 2020, American Chemical Society.[108] Copyright 2019, American Chemical Society.

boost overall battery performance. Defect engineering refines the electronic structure and reaction activity by meticulously controlling defect types and concentrations, thereby improving capacity and cycling stability. While these strategies have yielded impressive advancements in VO_2 performance, several technical hurdles persist. Developing composite material systems and exploring how defect engineering affects the electrochemical properties of VO_2 remain crucial. Addressing these challenges is pivotal to advancing the practical application of VO_2-based cathodes in AZIBs.

2. Crystal structure and morphology of VO_2

Vanadium-based cathode materials exhibit rich valence states and diverse crystal structures. These features enable multi-electron transfer, maintain local electrical neutrality, and reduce polarization caused by zinc ion embedding. As a result, they deliver excellent zinc storage performance. Vanadium oxide compounds such as V_2O_3, VO_2, V_2O_5, V_6O_{13}, V_3O_7, and V_5O_{12} have shown significant potential for zinc storage.[48] Among them, VO_2 stands out due to its unique and stable crystal structure. This structure allows efficient insertion and extraction of Zn^{2+} ions, resulting in a high theoretical specific capacity, good cycle stability, and high energy and power density. In addition, VO_2 has tunnel and layer structures in which vanadium oxygen layers are stacked on top of each other by weak van der Waals forces. This structure provides a natural pathway for the embedding and deembedding of Zn^{2+} ions, allowing ions to move freely between layers. The crystalline

structure of VO_2 is capable of maintaining a high degree of stability in the processes of Zn^{2+} insertion and extraction. This is due to the good flexibility and plasticity of the VO_2 structure, which can adapt to the lattice changes caused by ion embedding and deembedding, thus effectively reducing the destruction of the material structure and capacity attenuation. These properties make VO_2 an ideal cathode material for AZIBs.[49]

2.1 Crystal structure of VO_2

The diversity of crystal structures of VO_2 has made it a focus of research among the vanadium oxide system. Numerous crystal structures have been studied for VO_2, including tetragonal VO_2(A), monoclinic VO_2(B, D, M), and rutile VO_2(R) (Fig. 2).[50] In spite of the fact that the crystal structures of VO_2 differ greatly according to the coordination of V and O, the open framework and the coordination of O are remarkably similar. In addition to enriching the physical and chemical properties of VO_2, the rich and diverse crystal structures of VO_2 also provide broad avenues for its innovative applications in multiple fields like energy storage.[51] The crystal structure of tetragonal VO_2(A) is relatively rare when compared to other crystal structures of VO_2. As a result of its lattice arrangement, VO_2(A) can only be synthesized under certain specific synthesis conditions, as a result of its specific symmetry.[52] Due to the fact that relatively few studies have been conducted on VO_2(A), its physical and chemical properties are not yet fully understood. While research continues to deepen, people gradually begin to realize that VO_2(A) may be able to play a role in certain specific fields where the material has potential applications.

Monoclinic VO_2(B, D, M) is the most common crystal structure type in VO_2. As a result of its good ion conductivity and stability, VO_2(B) has attracted a great deal of attention. The crystal structure of VO_2(B) provides excellent ion conduction properties, making it a potential energy storage material. In the structure of VO_2(B), the V^{4+} ions represent the body center position with each V atom surrounding an oxygen octahedron (VO_6), which shares edges with the V^{4+} ions. VO_2(B) is a space group $P2_1/c$, lattice parameters are $a = 0.575$ nm, $b = 0.452$ nm, $c = 0.538$ nm, $\beta = 122.6°$ allowing for layered structures suitable for ion storage.[52] Using a hydrothermal method and a rapid multi-wave reaction process, Pinnock *et al.* synthesized tunnel-shaped VO_2(B).[53] VO_2(B) obtained by the multi-wave reaction process (Fig. 3a) can be decomposed into nanorods and clusters, and the hydrothermal synthesis rule produces nanorods with uniform morphology. In Fig. 3b, Zn^{2+} intercalated VO_2(B) nanorods are embedded and released along *b* and *c*. The X-ray diffraction (XRD) spectra of the two synthesized materials are similar, but the multiwave reaction is highly crystallized. According to the rate performance diagrams (Fig. 3c), VO_2(B) exhibits excellent energy storage properties due to its high

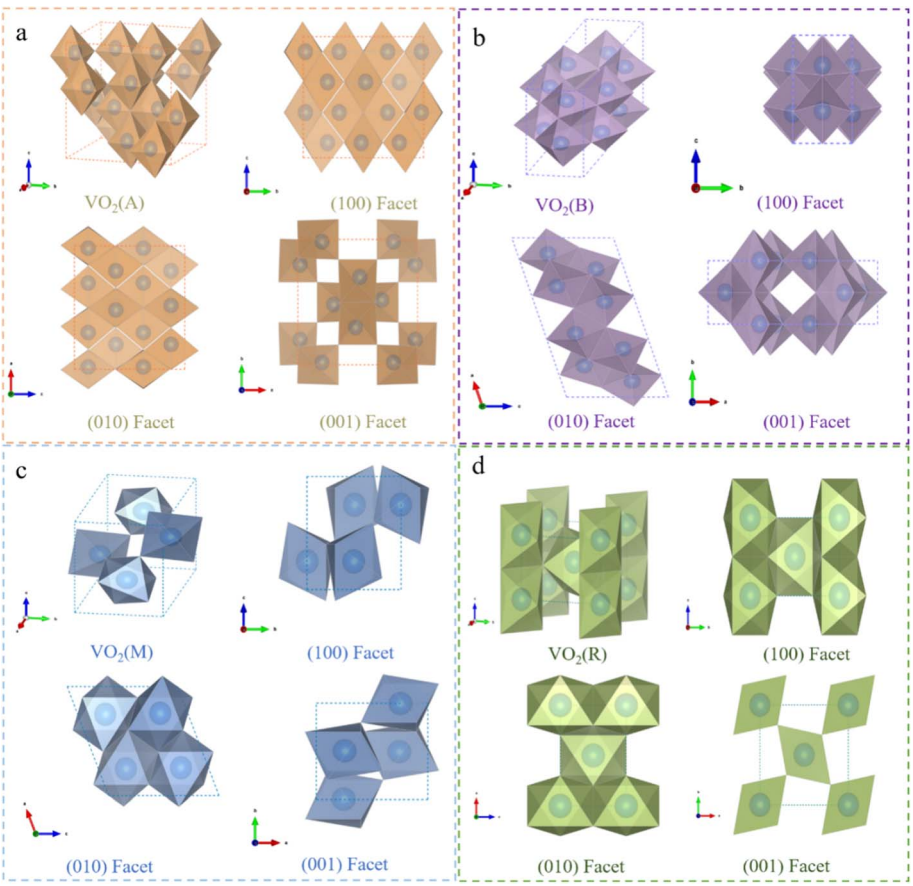

Fig. 2 The lattice structures of VO_2: (a) VO_2(A), (b) VO_2(B), (c) VO_2(M), and (d) VO_2(R), each viewed from different facets.

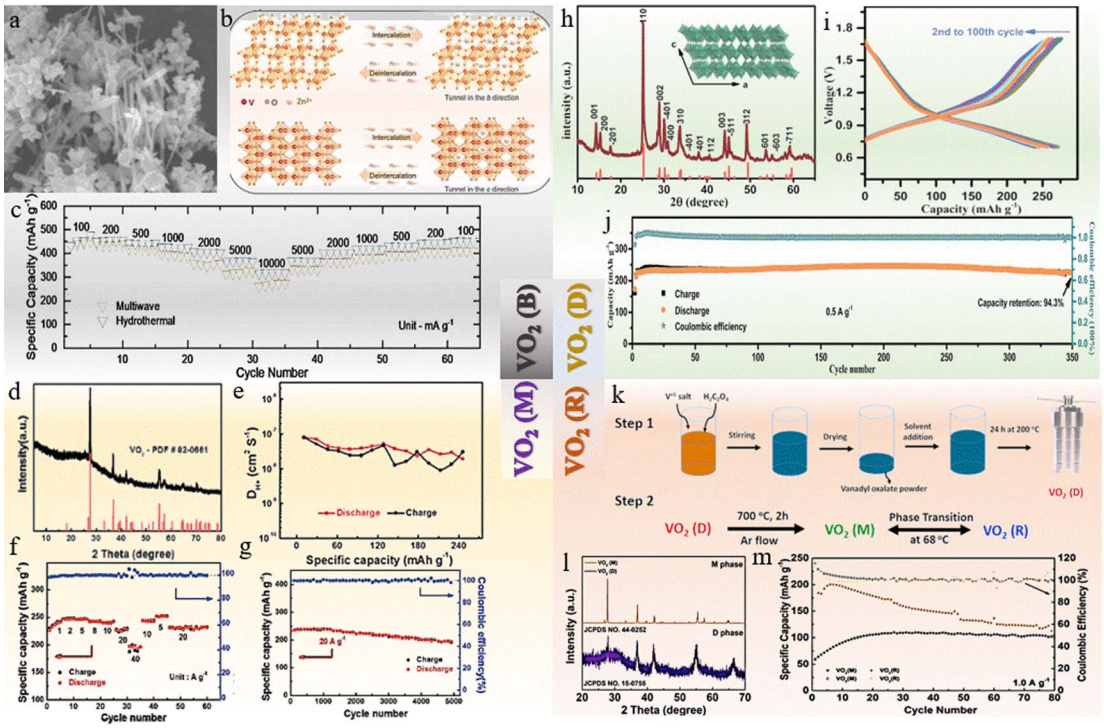

Fig. 3 (a) SEM images of multiwave digested VO_2(B), (b) schematic of Zn^{2+} (de)intercalation in VO_2(B) nanorods projected along the *b*- and *c*-directions, and (c) rate capacity tests for AZIBs, with cathodes synthesised *via* hydrothermal and multiwave synthesis approaches.[53] Copyright 2025, the Royal Society of Chemistry. (d) XRD pattern of VO_2(M), (e) H^+ diffusivity *vs.* specific capacity, (f) rate capability at varying current densities and corresponding coulombic efficiencies, and (g) extended cycling performance and the corresponding coulombic efficiency at 20 A g^{-1}.[56] Copyright 2022, the Royal Society of Chemistry. (h) XRD pattern of VO_2(D), (i) discharge–charge profiles of the VO_2(D) electrode obtained at a current density of 100 mA g^{-1} and (j) cycling performance at a current density of 0.5 A g^{-1}.[57] Copyright 2018, the Royal Society of Chemistry. (k) Schematic of the VO_2(M) hollow sphere fabrication processes. (l) XRD pattern of VO_2(D) and (m) the cycling performance of the VO_2(M) and VO_2(R) cathodes at 1.0 A g^{-1}.[59] Copyright 2024, Elsevier.

specific capacity and good rate performance. This enhancement is attributed to the morphology formed in the hydrothermal samples, increased oxygen vacancies and higher V^{4+} concentrations, which may contribute to more efficient Zn^{2+} ion intercalation compared to multiwave reactor samples.

VO_2(M) is another monoclinic variation that has received much attention in the recent past. There is a doubling of the unit cell in the M phase of VO_2 as vanadium atoms are paired along the chain, resulting in a doubling of the vanadium atoms. Interestingly, the vanadium atoms have a dislocated lateral displacement, while the oxygen octahedron is twisted and rotated as well.[54] The crystal structure of VO_2(M) undergoes significant transformation with temperature variation, leading to abrupt changes in its physical properties, such as electrical resistance. With its properties, VO_2(M) is an excellent choice for the preparation of temperature-controlled materials, such as smart windows.[55] Jiang's group oxidized V_2O_5 with H_2O_2 and compounded it with carbon nanotubes to obtain VO_2(M)/CNT films.[56] XRD peaks of the obtained product match those of standard card VO_2(M) (Fig. 3d), proving that VO_2(M) was successfully synthesized. Through the carefully designed three-dimensional porous structure, VO_2 particles can be dispersed well, promoting electrolyte transmission, relieving strain during ion insertion, and reducing by-product formation. In AZIBs, it has a fast ion transmission rate of 10^{-7} (Fig. 3e), exhibits ultra-high rate performance (Fig. 3f), and maintains a capacity of 232.6 mA h g^{-1} at a high current density of 20 A g^{-1}. AZIB cathode materials based on VO_2(M) exhibit excellent electrochemical performance, providing a potential strategy for designing high-performance cathodes.

In addition to VO_2(B) and VO_2(M), VO_2(D) is also a variant of the monoclinic system, which is also referred to as VO_2(D). Despite the fact that VO_2(D) has been less studied, it has been demonstrated that under certain conditions it may have unique physical and chemical properties. Consequently, in the future, with the increased depth of scientific research, it is expected that people will gradually become aware of the potential application value of VO_2(D). Wei *et al.* hydrothermally reacted ammonium vanadate with formic acid to obtain VO_2(D).[57] The XRD spectrum of the measured sample matches that of the VO_2(D) standard card (Fig. 3h), demonstrating successful synthesis of VO_2(D). It is used as a cathode material to measure electrochemical properties. At a current density of 0.1 A g^{-1}, the specific capacity can reach 265 mA h g^{-1} and still deliver 249 mA h g^{-1} after 100 cycles (Fig. 3i). VO_2(D) can also maintain 94.3% after 350 cycles at 0.5 A g^{-1} (Fig. 3j), demonstrating its high zinc storage capacity and long cycle stability. At the time of charging to 1.4 V, the (001) crystal surface of XRD expanded to

12.6 Å, which was consistent with the reported layered vanadium oxide $V_2O_5 \cdot nH_2O$, and no reversible disappearance or appearance occurred in the subsequent charging and discharging processes, so it is believed that this was a phase transition reaction. After a series of characterization studies such as *in situ* XRD, it is proved that the material transforms from VO_2(D) to $V_2O_5 \cdot H_2O$ in the first cycle, thus realizing stable zinc storage. During the phase transition from the ordered structure of VO_2 to the disordered structure of V_2O_5, a unique bilayer lamellar structure is formed, which is composed of double chains stacked face-to-face. It is particularly noteworthy that this newly formed phase plays a crucial role in subsequent electrochemical cycling and exhibits excellent flexibility, enabling it to adaptively adjust the ion diffusion paths to effectively accommodate volume changes, thereby demonstrating remarkable zinc storage stability.

The rutile structure of VO_2(R) is the stable structure of VO_2 when heated above a certain temperature. A phase transition will occur between monoclinic variants such as VO_2(M) and rutile VO_2(R), accompanied by significant changes in the crystal structure and a sudden change in physical properties. Because the vertices and edges of the VO_6 octahedron are shared, the VO_2(R) octahedron forms a more complex network structure. The lattice constants of VO_2(R) are $a = b = 0.451$ nm and $c = 0.304$ nm, and it belongs to the $P4_2/mnm$ space group.[58] It is important to note that VO_2(R) is a substance that has excellent chemical and thermal stability, making it suitable for use in harsh environments such as high temperatures and high pressures. Therefore, rutile VO_2(R) can be used for a wide range of applications, including ceramics, coatings, catalysts, and many others. Using oxalic acid and vanadium oxalate, Aydogdu *et al.*[59] produced vanadium oxalate. In an argon atmosphere, they calcined the filtered and dried product and successfully converted VO_2 from the M phase to the R phase, which is suitable for use in AZIBs. VO_2(R) exhibits higher specific capacity/power density and lower charge transfer resistance due to its metal-insulator transition behavior, which result in improved electrochemical performance.

2.2 Morphology of VO_2

The development of VO_2 materials is frequently guided by morphology engineering design. VO_2 of the same crystal form can have different morphologies when synthesized using different synthesis strategies. Cathode materials with different morphologies, however, have different cycling stabilities.[60–62] On the one hand, it is possible to shorten the diffusion path of Zn^{2+} using some morphological structures, which facilitates the rapid insertion/extraction of Zn^{2+}. On the other hand, some materials with a dense stacking or irregular morphology may suffer from performance degradation during the cycle as a result of structural damage, leading to degradation of performance.[63] A new type of VO_2 nanosheet has been successfully developed by Cao *et al.*[64] with high uniformity and a circular structure. With a diameter of about 500 nm, a thickness of about 50 nm, and a hole in the middle, the nanosheet resembles an ancient coin (Fig. 4a–c). Circular nanosheets can be divided into middle and outer parts based on their curvature. The microcrystal's middle region can be considered a smaller circular nanosheet with a higher curvature than its outer region, so it has a higher surface energy than its outer region. Once equilibrium is reached, the structure remains highly stable. For AZIBs with VO_2 as the cathode, a reversible capacity of 394 mA h g^{-1} is achieved at 0.1 A g^{-1}. According to Bai *et al.*,[65] curled VO_2(B) nanosheets were produced by adding hydrogen peroxide (H_2O_2) to the commercial V_2O_5 precursor (Fig. 4d–f). The insertion and extraction of Zn^{2+} in/from the precursor do not compromise its structural integrity. The application of VO_2(B) nanosheets in AZIBs showed good electrochemical performance (400.2 mA h g^{-1} at 0.5 A g^{-1}).

Hierarchical nanoflowers with a larger specific surface area can provide more active sites for zinc storage. A VO_2(B) nanosheet with a petal-like folded top was reported by Bai *et al.* (Fig. 4g–i).[66] Electrolytes enter through the gaps between the nanosheets, bringing more ions and facilitating faster storage. The higher pseudocapacitive contribution and partial diffusion in VO_2(B) enhance its electrochemical activity, accelerate electron transfer kinetics, and improve electronic conductivity. VO_2(B) shows a significant capacity of 301.7 mA h g^{-1} at 1 A g^{-1}. In an *in situ* self-conversion method, Deng *et al.*[67] synthesized VO_2 with a hierarchical flower-like structure by electrochemically improving the activity of argon-treated VO_2 (AVO) microspheres (Fig. 4j–l). The AVO cathode material with a hierarchical flower-like structure and high crystallinity enables fast ion transfer, thus exhibiting fast reaction kinetics. This AZIB achieves a capacity of 446/361 mA h g^{-1} at 0.1/5 A g^{-1}. He *et al.*[68] developed high-performance AZIBs by exposing different crystal faces of VO_2(B) to an aqueous solution. By directionally aligning VO_2(B) channels along the *c*-axis, they achieved rapid ion transport and enhanced performance.

3. Energy storage mechanism of VO_2

Research on various energy storage systems focuses on understanding their reaction mechanisms, making the development of AZIBs one of the most significant challenges. VO_2-based AZIBs, with their complex electrolyte system and various forms of VO_2, involve more intricate reaction processes. During discharge, zinc from the zinc sheet loses electrons, forming Zn^{2+} ions that enter the electrolyte. Subsequently, Zn^{2+} ions migrate to the cathode, inducing the reduction of V^{4+} to V^{3+} upon insertion. In the charging phase, Zn^{2+} ions leave the cathode and return to the electrolyte, while V^{3+} is oxidized back to V^{4+}. After migration, V^{4+} precipitates onto the zinc electrode. There are several types of VO_2-based cathode materials, each with distinct characteristics for zinc storage in AZIBs (Fig. 5). These materials can be categorized into three primary energy storage mechanisms: (1) Zn^{2+} insertion/extraction; (2) H^+/Zn^{2+} co-insertion/extraction; and (3) chemical reaction mechanisms.

3.1 Zn^{2+} insertion/extraction mechanism

Among the new technologies for storing energy, AZIBs have a number of energy storage mechanisms that are similar to

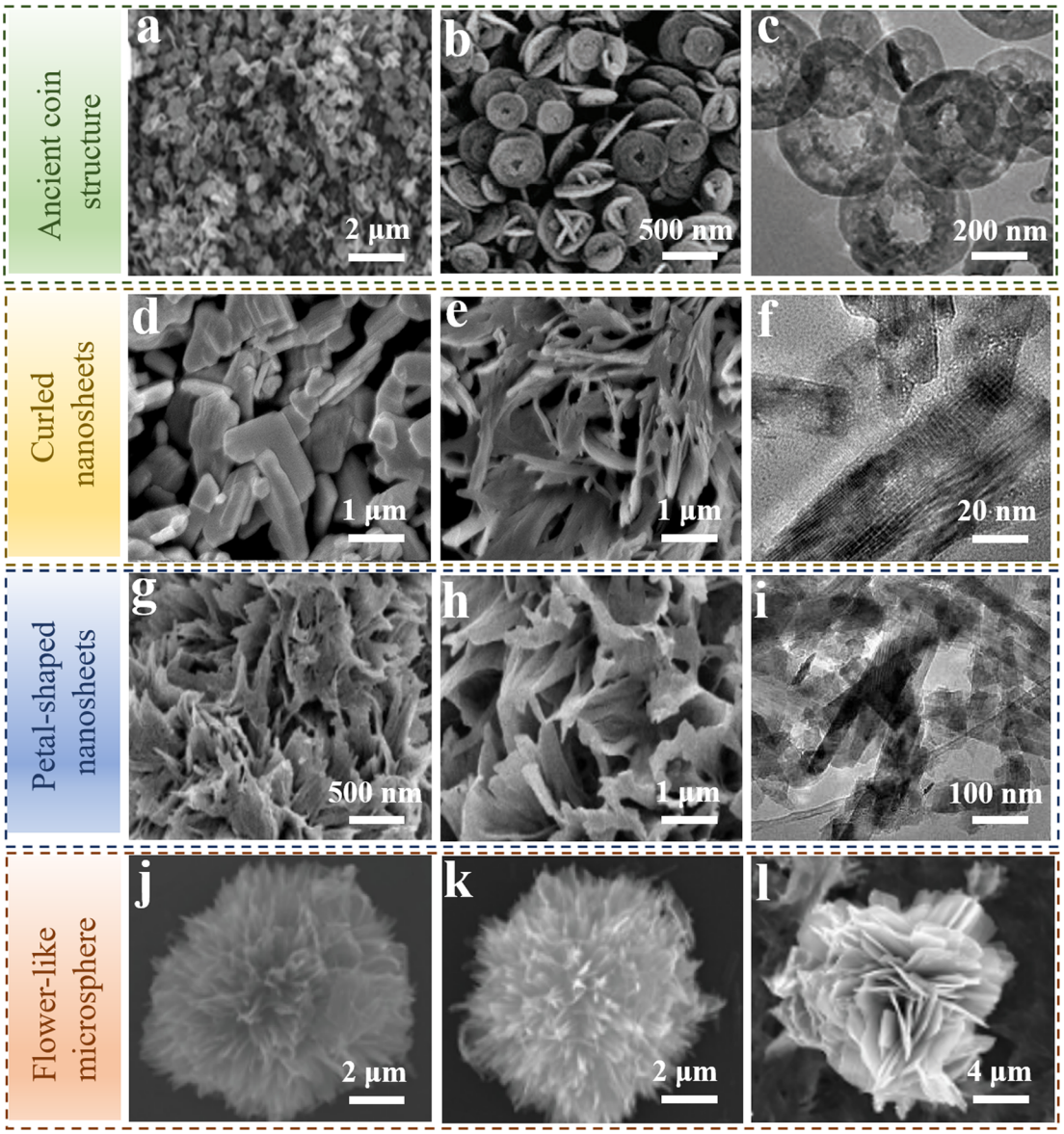

Fig. 4 (a–c) VO_2 nanosheets with an ancient coin structure.[64] Copyright 2020, Wiley-VCH GmbH. (d–f) Curled VO_2 nanosheets.[65] Copyright 2023, Elsevier. (g–i) Petal-shaped folded VO_2 nanosheets.[66] Copyright 2022, Elsevier. (j–l) Hierarchical flower-shaped VO_2 nanosheets.[67] Copyright 2023, Wiley-VCH.

those of traditional lithium-ion batteries, but also have some differences as well. In AZIBs, VO_2 is considered to be one of the most important types of cathode materials since it exhibits unique energy storage properties. Zinc metal at the negative electrode undergoes an oxidation reaction during the discharge process, resulting in the release of Zn^{2+} accompanied by the release of electrons as a result of the oxidation reaction.[69] Through the electrolyte, these Zn^{2+} ions migrate to the surface of the VO_2 positive electrode and become embedded in its lattice structure, thus becoming embedded in the lattice structure of VO_2. Vanadium ions (V) in VO_2 are usually partially reduced from a higher valence state (such as V^{4+}) to a lower valence state (such as V^{3+}) during this process, as a result of which a Zn_xVO_2 form is formed, and thus charge storage is achieved. By passing electrons through an external circuit, electrons flow from the anode to the cathode, converting chemical energy into electrical energy. In contrast, electrons flow through an external circuit, connected to an external power source, from the cathode to the anode during the charging process. The embedded Zn^{2+} ions in the VO_2 cathode are oxidized and re-released, returning to the Zn^{2+} state. After migrating through the electrolyte to the negative electrode surface, these zinc ions are reduced to metallic zinc, completing the charge release process. This process will gradually return the lattice structure of VO_2 to its original state, preparing it for the next discharge.

To investigate the storage behavior of Zn^{2+} in VO_2(B), Ding *et al.*[70] prepared VO_2(B) nanofibers by a hydrothermal method

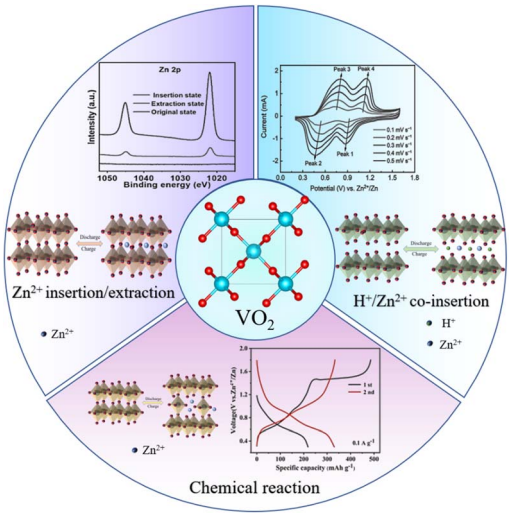

Fig. 5 Schematic diagram of three energy storage mechanisms of a VO_2-based cathode for AZIBs.[69] Copyright 2019, American Chemical Society.[72] Copyright 2021, Wiley-VCH.[74] Copyright 2021, Elsevier.

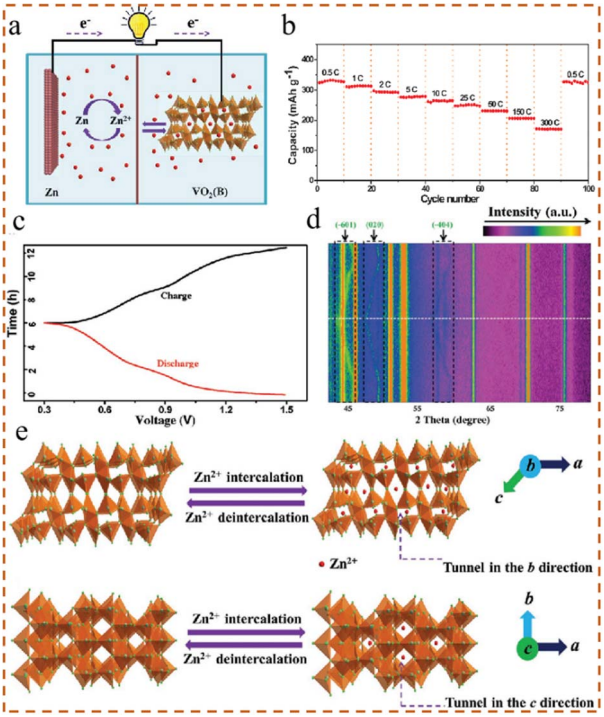

Fig. 6 (a) Crystal structure of VO_2 and battery schematic. (b) Rate performance of VO_2. (c) Charge–discharge curve of VO_2 at 0.5C. (d) *In situ* XRD pattern of VO_2. (e) Schematic diagram of Zn^{2+} embedded in different crystal planes of VO_2.[70] Copyright 2018, Wiley-VCH.

(Fig. 6a), which showed excellent rate performance when embedded with Zn^{2+}. After cycling the current at a high level for a considerable period of time, it was possible to restore the original capacity (Fig. 6b) when the current was reduced to a small level. Fig. 6c shows a typical charge–discharge curve at 0.5C. *In situ* XRD measurements were performed (Fig. 6d), and three strong peaks were observed at 45.1°, 49.2° and 59.1°, which correspond to the (−601), (020) and (−404) crystal planes of VO_2(B), respectively. The 2D profiles of the *in situ* XRD patterns during the charge and discharge process are completely symmetrical, indicating that Zn^{2+} can be easily embedded and extracted from VO_2(B) nanofibers. Zn^{2+} embedding into VO_2(B) from different crystal planes is represented by the changes in crystal planes (Fig. 6e). There is a slight increase in the lattice spacing of VO_2(B) during complete Zn^{2+} embedding, confirming that the structure of VO_2(B) changes little during the process of Zn^{2+} embedding. During the process of charging from 0.3 V to 1.5 V, these peaks reversibly move back to the initial positions, further proving that the VO_2(B) tunnel has good stability for zinc storage. In the discharge process from about 0.75 V to 0.3 V, a new peak appeared at 58.8°, which is also reversible, coinciding with the appearance of a second redox peak at about 0.65 V in the CV curve. As a result, the electrochemical reaction can be summarized as follows:

$$\text{Cathode: } xZn^{2+} + VO_2 + 2xe^- \leftrightarrow Zn_xVO_2 \quad (1)$$

$$\text{Anode: } Zn \leftrightarrow Zn^{2+} + 2e^- \quad (2)$$

$$\text{Overall: } VO_2 + xZn \leftrightarrow Zn_xVO_2 \quad (3)$$

3.2 H^+/Zn^{2+} co-insertion/extraction mechanism

In cathode materials, H^+ and Zn^{2+} insert at different sites, resulting in more efficient energy storage and release. The study of the scientific principles and application prospects of the co-insertion/extraction mechanism of H^+/Zn^{2+} can open up new avenues for the development of battery technology. Nevertheless, further research and exploration are needed to realize this mechanism's practical application.[71] H^+/Zn^{2+} co-insertion/extraction is related to different vanadium oxides, and the composition of the electrolyte will also affect chemical reactions. A hydrated vanadium dioxide (O_d-HVO@PPy) coating with polypyrrole (PPy) was synthesized by Zhang *et al.* (Fig. 7a).[72] Using a High Resolution Transmission Electron Microscope (HRTEM), O_d-HVO@PPy has a lattice spacing of 0.343 nm, which comes from the (110) plane of $VO_2 \cdot xH_2O$ nanocrystals. Vanadium oxide does not dissolve when wrapped in PPy, as shown in Fig. 7b. XPS and EPR measurements show that the O_d-HVO@PPy material has an oxygen defect structure (Fig. 7c). The initial specific capacity of the O_d-HVO@PPy electrode is as high as 334 mA h g^{-1} at 2 A g^{-1}, which is mainly attributed to the presence of a polypyrrole protective layer to prevent vanadium oxide from dissolving (Fig. 7d). For further investigation of the electrochemical mechanism of O_d-HVO@PPy electrodes during cycling, *ex situ* XRD and XPS characterization was used (Fig. 7e and f). *Ex situ* XPS characterization reveals symmetry during the charge and discharge processes, indicating that O_d-HVO@PPy is reversible during these processes. During the cycle, another significant peak was observed at 12.4°, which was identified as $Zn_4(OH)_6SO_4 \cdot xH_2O$. During the deep discharge process, intensity increased until it reached a maximum value. During the charging process, it decreased until it disappeared in the fully

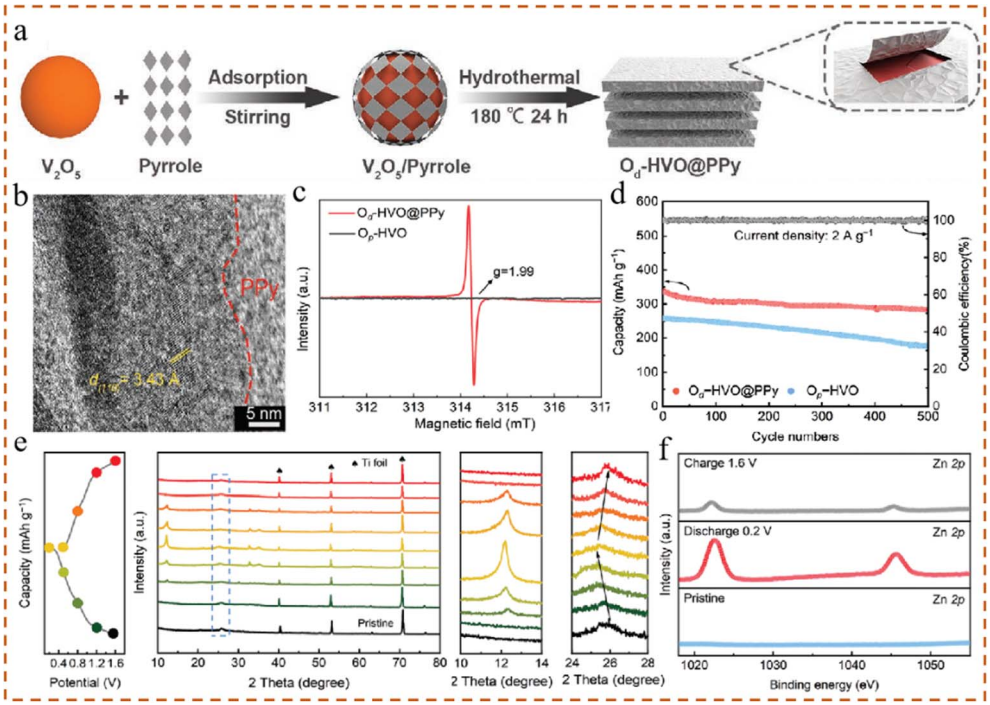

Fig. 7 (a) Schematic diagram of the synthesis of O_d-HVO@PPy, (b) HRTEM of O_d-HVO@PPy, (c) electron paramagnetic resonance of O_d-HVO@PPy, (d) long-cycle curves of O_d-HVO@PPy and O_d-HVO electrodes at 2 A g^{-1}, (e) *ex situ* XRD of the O_d-HVO@PPy electrode in selected states of the 2nd cycle, and (f) XPS spectra of Zn 2p in the 2nd cycle.[72] Copyright 2021, Wiley-VCH.

charged state with a high degree of cyclic reversibility. As the OH^- is extracted from water, H^+ participates in embedding, and OH^- forms $Zn_4(OH)_6SO_4 \cdot xH_2O$ with Zn^{2+}.

3.3 Chemical reaction mechanism

During the discharge process, H^+/Zn^{2+} co-insertion into the VO_2 lattice triggers a change in its chemical structure, thereby generating a new compound. A new material with unique energy storage properties is formed by reshaping the original VO_2 crystal morphology. This new compound, formed by the embedding process, effectively participates in the reversible storage and release cycle of energy during the subsequent charging phase.[73] The reversible formation of new products is an important symbol to identify the mechanism of chemical transformation. If the new product can be reversibly formed and disappear during charge and discharge, this is usually due to the H^+/Zn^{2+} or Zn^{2+} insertion/extraction mechanism. However, if the new product, once formed, directly participates in the subsequent charge and discharge process in this form and does not disappear reversibly, this situation should be classified as a chemical transformation mechanism. The reaction path of VO_2 is a dynamic equilibrium result of the interaction of experimental conditions (ionic environment and preparation process), material properties (crystal phase and surface state) and kinetics (rate and diffusion barrier) and needs to be further verified by specific experiments (such as *in situ* characterization and crystal relative ratio). Using a sol–gel thermal method, Ding *et al.*[74] have prepared VO_2(B) nanorods by hydrothermally treating V_2O_5 and ethylene glycol for hydrothermal treatment. XRD measurements under various zinc ion storage states showed that when the zinc ion storage state was charged to 1.4 V, the intensity of the 12.2° characteristic peak began to increase significantly. Upon reaching the maximum value of 1.8 V, the characteristic peak density of VO_2(B) reached its maximum value, which indicates that VO_2(B) was completely converted (Fig. 8a). From the HRTEM images of the original VO_2(B), it can be observed that the lattice spacings of its (110) and (003) planes are 0.352 nm and 0.202 nm, respectively. After being fully discharged to 0.3 V, the lattice spacing of the (003) plane increases to 0.212 nm due to the insertion of some zinc ions. Moreover, the most direct evidence indicating the successful transformation is the emergence of a new lattice spacing of 0.419 nm on the (011) plane of $Zn_3(OH)_2V_2O_7 \cdot 2H_2O$. This is consistent with XRD, again demonstrating the formation of a new product of transformation. According to the charge–discharge curves of the initial two cycles of VO_2(B) nanorods at 0.1 A g^{-1} in a voltage range of 0.3–1.8 V, a long charging platform is observed when the voltage reaches about 1.5 V for the first time, but disappears with subsequent charging cycles, suggesting that an irreversible conversion reaction has occurred during the first charging process. After the first charge reached 1.8 V, the discharge specific capacity also increased, showing that the active material obtained after the conversion is able to store more zinc ions (Fig. 8b). The reversible capacities of VO_2(B) nanorods are 327, 319, 287, 210 and 130 mA h g^{-1} at 0.5, 1.0, 2.0, 5.0 and 10.0 A g^{-1}, respectively (Fig. 8c). According to the XPS graph of Zn (Fig. 8d), when the electrode is charged to 1.8 V, the signal

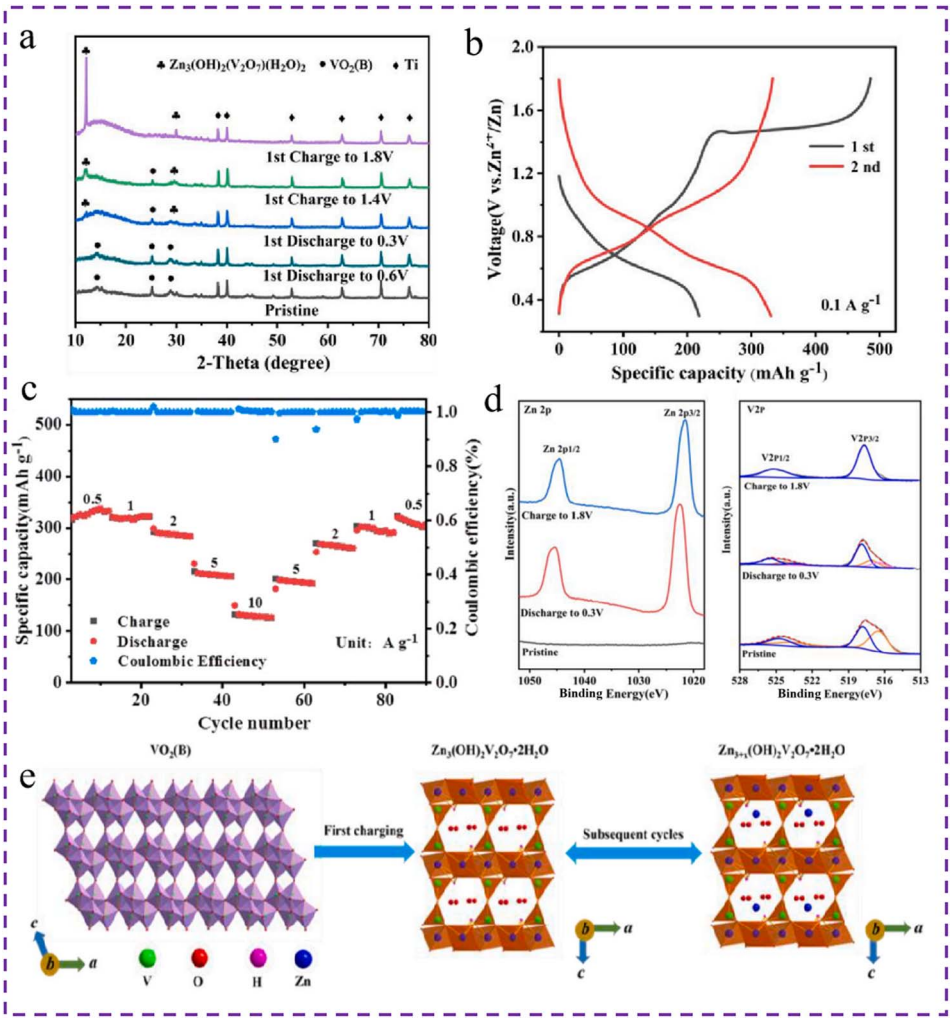

Fig. 8 (a) XRD pattern of VO_2(B) during charge and discharge, (b) charge–discharge curves of VO_2(B) at 0.1 A g^{-1} for the 1st and 2nd cycles, (c) rate performance diagram of VO_2(B), (d) XPS of Zn 2p and V 2p under different states of VO_2(B), (e) schematic diagram of the energy storage mechanism of Zn/VO_2(B) during the 1st and 2nd cycles.[74] Copyright 2021, Elsevier.

peak of Zn 2p is still present. This indicates that zinc-containing compounds were subjected to *in situ* conversion during the initial charging process, and the measured V 2p also corresponds to the embedding of Zn^{2+} in the electrode. As a result of various characterization analyses and electrochemical tests, it was confirmed that the *in situ* conversion reaction product is flaky $Zn_3(OH)_2V_2O_7{\cdot}2H_2O$ (Fig. 8e).

4. Critical issues of VO_2-based cathodes

Due to its excellent electrochemical properties, VO_2 has become a promising AZIB cathode material. Despite the strong potential of VO_2-based cathode materials, there are still problems such as dissolution, by-product production and ionic diffusion kinetics limitations, which lead to differences between the experimental and theoretical capacity of VO_2, preventing their widespread commercial application (Fig. 9). These issues primarily arise from the inherent complexities and challenges associated with vanadium oxide itself. To enable the broad use of VO_2-based cathode materials in AZIBs, extensive research is required to address and overcome these obstacles.

4.1 Dissolution

The crystal structure of VO_2 undergoes significant alterations during the dynamic process of insertion/extraction of Zn^{2+}. As Zn^{2+} is inserted into the lattice, the VO_2 structure gradually adapts to accommodate these ions. However, once the amount of embedded Zn^{2+} reaches a certain threshold, the crystal structure can no longer maintain its integrity and stability, leading to collapse and eventual dissolution into the electrolyte. This process is further complicated by the simultaneous embedding of water molecules, which interact with oxygen atoms in the V–O bonds. These interactions create new bonding patterns that weaken the original V–O bonds, destabilizing the crystal structure of VO_2. As the V–O bonds continue to weaken, VO_2 reaches a critical point where it dissolves into the electrolyte due to the continuous embedding of water molecules. Additionally, the charging and discharging cycles can induce phase transitions in VO_2. These transitions significantly alter

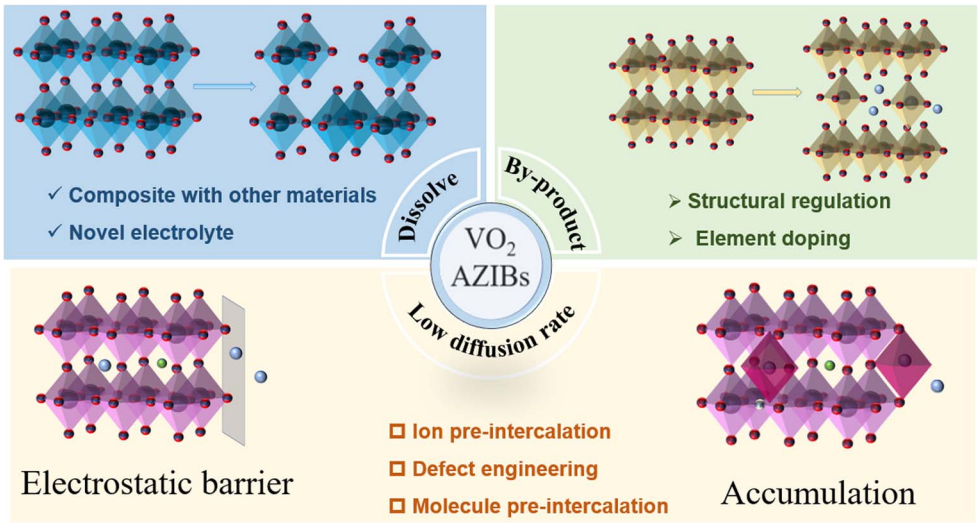

Fig. 9 The main problems and strategies of VO_2-based cathode materials for AZIBs.

both its crystal structure and chemical properties, further compromising its stability. After phase changes, some VO_2 becomes more soluble in the electrolyte, exacerbating the dissolution issue. Consequently, the insertion and extraction of Zn^{2+}, the incorporation of water molecules, and the phase transition phenomena contribute to the loss of the crystal structure of VO_2, leading to its eventual dissolution.[46] To enhance the stability and anti-dissolution properties of VO_2, further in-depth research into its crystal structure and chemical properties is essential.

4.2 Generation of by-products

When an aqueous electrolyte comes into contact with VO_2, a reactive process occurs, leading to the formation of various by-products depending on the type of electrolyte used. These by-products, often in the form of hydroxides, salts, and other compounds, can significantly affect the electrochemical performance of VO_2. Initially, the by-products may occupy the active sites intended for Zn^{2+} storage, which reduces the battery's capacity. The deposition of by-products on the electrode surface can also hinder the diffusion of Zn^{2+}, impacting the battery's charge and discharge efficiency as well as its cycle stability. As the deposition of by-products continues, they can form a thick passivation layer, which further reduces the electrochemical performance by obstructing successful interaction between Zn^{2+} and VO_2. Current research on AZIBs must focus on addressing these adverse reactions between VO_2 and aqueous electrolytes, with the goal of reducing by-product formation.[75] To enhance the overall performance of AZIBs, optimizing the electrolyte composition and electrode structure and exploring new electrode materials are essential areas for future development.

4.3 Limited ion diffusion kinetics

As for the mechanism of reaction in AZIBs, it is certain that whatever mechanism is used, the reaction always involves the conversion of zinc in the zinc negative electrode to Zn^{2+}, which is then released into the electrolyte, migrates to the positive electrode, and interacts with the cathode. Due to the fact that Zn^{2+} is a divalent cation, it carries two units of positive charge at once. There is a strong electrostatic effect that Zn^{2+} has in an electric field because of this high charge state. Due to this electrostatic effect, it is easy for Zn^{2+} to interact strongly with negatively charged anions in the electrolyte or electron clouds in the cathode material during the migration process. Zn^{2+} cannot freely diffuse due to this interaction, which acts like an invisible barrier. More complicated, however, is that the lattice structures of different positive electrode materials are unique, and each of these lattice structures corresponds to a significant difference in the diffusion rate of Zn^{2+} within the positive electrode materials. Cathode materials are capable of undergoing phase transitions, lattice strains, or dissolution during a cycle of operation.[52,75] Thus, the structure of the cathode material could become unstable, further reducing the diffusion rate of Zn^{2+}.

4.4 Others

The inadequate electrochemical performance of cathode materials is also one of the key factors that are hindering the development of AZIBs due to the low electrochemical performance. Due to their poor conductivity and low electrochemical activity, some materials are prone to slow electrode reaction rates and reduced battery charge and discharge efficiency as a result. During the charge and discharge process, it is possible that the cathode material will undergo phase changes, lattice strains, and a variety of other changes that will challenge its structural stability and will further affect the diffusion of Zn^{2+} as well as the ability of the battery to charge and discharge. For the purpose of overcoming these challenges, the structure, composition, and preparation process of the material are optimized to increase the conductivity, electrochemical activity, and structural stability of the material, while reducing dissolution and by-product generation and improving the diffusion rate of

Zn^{2+} and electrochemical performance of the material. In addition, due to different electrochemical windows, different electrolytes, temperature and other influencing factors, the reported VO_2 cathode capacity varies greatly. Therefore, it is necessary to standardize the test conditions, optimize the electrolyte and electrode design, consider the temperature effect, and conduct a comprehensive comparison and analysis. This will help promote the application and development of VO_2 cathodes in areas such as zinc-ion batteries and realize commercialization at an early date.

5. Optimization strategies of VO_2-based cathodes

The poor electrochemical performance of cathode materials remains a significant challenge for the development of AZIBs. While VO_2 is often considered an ideal cathode material for AZIBs, it still faces several issues, including slow reaction kinetics, low electronic conductivity, structural instability, and vanadium dissolution. To address these challenges, various design strategies have been proposed to enhance the electrochemical performance of VO_2. These strategies include ion/molecule pre-intercalation, the use of composite materials, defect engineering, and elemental doping (Fig. 10). By adopting these optimization strategies, the electrochemical performance of VO_2 can be improved. However, it is crucial to select an appropriate strategy based on the specific structure and needs of the system to achieve optimal results.

5.1 Ion pre-intercalation

Electrostatic interactions between Zn^{2+} and cathode materials prevent further insertion and extraction of Zn^{2+} when Zn^{2+} ions are embedded in cathode materials. Additionally, it will cause the material to collapse and dissolve in the electrolyte, resulting in decreased electrochemical performance. Research has shown that the embedding of foreign ions in VO_2 materials not only stabilizes the crystal structure by acting as a "pillar", but also weakens electrostatic interactions during the Zn^{2+} embedding process, preventing the structure from collapsing after Zn^{2+} embedding and extraction, thus improving electrode cycle stability.[76,77] The microwave-assisted hydrothermal method was used by Li *et al.*[78] to prepare a nanosphere-cathode containing potassium ions (K^+) embedded in VO_2(B). As a pillar, K^+ has a large ionic radius of 0.138 nm, which greatly improves the diffusion rate of Zn^{2+}. The HRTEM image shows a lattice with a spacing of 0.62 nm, which corresponds well to the crystal plane (001) of monoclinic VO_2(B). The nanobelts also showed a lattice fringe of 0.58 nm, which corresponded to the (200) plane of the undoped VO_2(B). Due to the tunnel-like structure of VO_2(B), K^+ can be accommodated with minimal distortion in the lattice. The battery held a charge capacity of 373 mA h g^{-1} at 0.5 A g^{-1}.

The highly active transition metal Mn, which has a large ionic radius and high activity, is a suitable guest insertion ion.[79,80] After expanding the interlayer spacing as tunnel "pillars", the pre-inserted Mn^{2+} in the VO_2 lattice can store more Zn^{2+} and also provide faster channels and paths. Additionally, metal ions will form oxygen vacancies inside the crystal, which can enhance conductivity and improve redox activity. An oxalic acid solution was added as a reducing agent after dispersing Mn^{2+} in a vanadium solution. MnVO nanobelts with Mn^{2+} pillars were successfully synthesized (Fig. 11a).[79] As can be seen from XRD, the phases of VO_2 and MnVO are completely consistent with the standard card, indicating that Mn^{2+} ions are doped into the VO_2 bulk phase without creating any new phases. In VO_2, Mn^{2+} ions are embedded in a tunnel structure composed of VO_6 octahedrons with shared edges and oxygen vertices. Zn^{2+} is stored abundantly in an extended tunnel structure that provides a fast transmission channel. Further, Mn^{2+} can improve the conductivity of the VO_2 main phase by optimizing its crystal structure and electron distribution. In comparison to VO_2 as the cathode material for AZIBs, the charge and discharge platform of MnVO is consistent with that of VO_2 (Fig. 11b), with a clear redox platform corresponding to the embedding of Zn^{2+}. The MnVO electrode exhibits excellent rate performance (Fig. 11c). Reversible capacities of 432, 418, 390, 364, 338, 281, and 187 mA h g^{-1} can be achieved at 0.1, 0.2, 0.5, 0.8, 1, 2, and 5 A g^{-1}, respectively. Furthermore, they explained the mechanism of insertion and extraction of Zn^{2+} (Fig. 11d). For insertion and extraction, Zn^{2+} ions combine with water to form hydrated zinc ions ($Zn(H_2O)_6^{2+}$). In this combination, the slow kinetics caused by the desolvation process can be suppressed. By optimizing the electronic structure, Mn^{2+} doping also improves the conductivity of the MnVO electrode. In addition, the increased interlayer spacing of MnVO reduces electrostatic interactions, facilitates the rapid transmission of Zn^{2+} within the tunnel, and minimizes irreversible side reactions, resulting in excellent rate and cycle performance. Metal ions can be embedded to maintain charge balance, prevent structural collapse, and improve conductivity. Liu *et al.*[81] introduced Na^+ and H^+ into VO_2 together. Na^+ can expand the tunnel, stabilize the

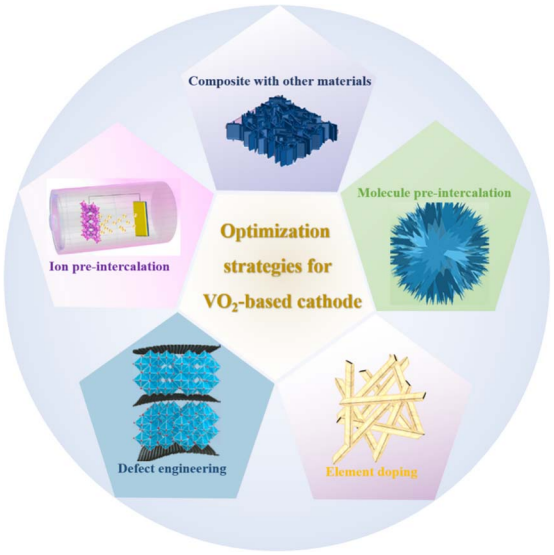

Fig. 10 Schematic diagram of the optimization strategy for VO_2-based cathode materials.[67] Copyright 2023, Wiley-VCH.[81] Copyright 2021, Elsevier.[98] Copyright 2024, American Chemical Society.[106] Copyright 2023, Elsevier.

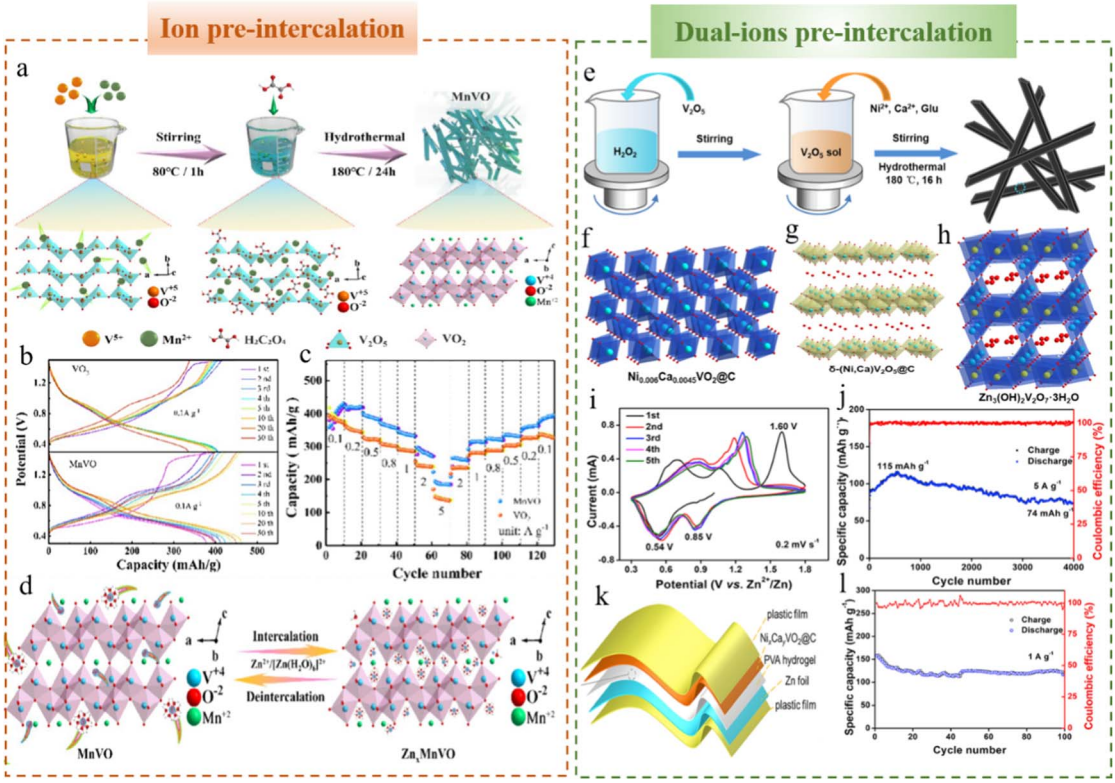

Fig. 11 (a) Schematic diagram of the synthesis of MnVO. (b) Charge–discharge curves and (c) rate performance curves of MnVO and VO_2. (d) Schematic diagram of Zn^{2+} insertion/extraction of MnVO.[79] Copyright 2023, American Chemical Society. (e) Schematic diagram of the synthesis of $Ni_{0.006}Ca_{0.0045}VO_2$@C. Structures of (f) $Ni_{0.006}Ca_{0.0045}VO_2$@C, (g) δ-(Ni,Ca)$V_2O_5$@C, and (h) $Zn_3(OH)_2V_2O_7\cdot 3H_2O$. (i) CV curve of $Ni_{0.006}Ca_{0.0045}VO_2$@C, (j) cycle diagram of $Ni_{0.006}Ca_{0.0045}VO_2$@C, (k) schematic diagram of the structure of a flexible quasi-solid-state battery, and (l) cycle performance diagram of the solid-state battery.[82] Copyright 2022, Elsevier.

crystal form, and prevent structural collapse when pre-embedded. The structural water surrounding Zn^{2+} also plays an important role, as it can act as a buffer to reduce electrostatic interactions between the ions. With its more stable crystal, it is capable of having an initial capacity of 156 mA h g^{-1} at 12 A g^{-1} and maintaining a capacity of 118 mA h g^{-1} after 3000 cycles.

The role of a single metal cation is often insufficient to maintain the stability of the material, and thus double metal cations are embedded into VO_2 through the pre-intercalation method in order to improve its electrochemical performance. The calcium ions have a larger ionic radius, which facilitates the expansion of interlayer spacing and the stabilization of crystal structures. Nickel ions can not only support a material but also enhance its conductivity. Zhao *et al.* synthesized double cation pre-intercalated vanadium dioxide ($Ni_{0.006}Ca_{0.0045}VO_2$@C) (Fig. 11e).[82] XRD analysis of the prepared material indicated that VO_2 was monoclinic in nature. The XRD spectrum revealed no peaks attributed to carbon, indicating that VO_2 and amorphous carbon were successfully prepared. Ca^{2+} and Ni^{2+} were successfully inserted, causing a slight positive shift in 2θ, indicating an enlarged interlayer. The first cycle CV curve of $Ni_{0.006}Ca_{0.0045}VO_2$@C shows an irreversible oxidation peak at 1.60 V, indicating that the vanadium(IV)-based oxide is *in situ* converted to a V_2O_5-based double-layer structure (Fig. 11f–h). The δ-V_2O_5-based double-layer structure gives the $Ni_{0.006}Ca_{0.0045}VO_2$@C electrode a higher specific capacity (433.8 mA h g^{-1} at 0.1 A g^{-1}) (Fig. 11i). $Ni_{0.006}Ca_{0.0045}VO_2$@C electrodes have a reversible capacity of 115 mA h g^{-1} at 5 A g^{-1} and can maintain 74 mA h g^{-1} after 4000 cycles (Fig. 11j). Under various charge and discharge conditions, the zinc storage mechanism of the $Ni_{0.006}Ca_{0.0045}VO_2$@C electrode was investigated by *ex situ* XRD. After the first charge to 1.4 V, vanadium(IV)-based oxide remains the main vanadium species. Upon initial charging to 1.6 V, the characteristic peaks of the VO_2-phase disappear, while those of the V_2O_5 phase emerge, coinciding with the charge plateau near 1.55 V. This observation confirms the effective phase transition achieved through electrochemical activation. In subsequent cycles, the zinc ion storage mechanism primarily involves reversible Zn^{2+}/H^+ co-insertion/extraction in the host lattice of double-layer structured δ-V_2O_5. During the charge–discharge process, a new phase of $Zn_xV_2O_5\cdot nH_2O$ was also detected due to the conversion reaction and H_2O co-insertion behavior. Fig. 11k and l show its application to a flexible quasi-solid-state battery. The first discharge specific capacity was 158 mA h g^{-1}, and it remained at 73.2% after 100 cycles, indicating long-term cycle stability.

5.2 Molecule pre-intercalation

By introducing molecules into the VO_2 material matrix in advance, as opposed to directly embedding cations, the intrinsic

crystal structure of VO_2 and the Zn^{2+} transport kinetics can be significantly regulated by forming chemical bonds or coordination with the main structural framework. Molecule embedding plays a crucial role as a "lubricant" in this process. Besides expanding the interlayer distance and creating favorable conditions for Zn^{2+} migration, it can also reduce the electrostatic interaction strength between the embedded Zn^{2+} and the active material by acting as a charge shielding layer. A mixture of NH_4VO_3 and polyacrylamide is combined with hydrochloric acid and hydrogen peroxide. After hydrothermal treatment, $VO_2 \cdot xH_2O$ and $(NH_4)_2V_{10}O_{25} \cdot 8H_2O$ can be obtained (Fig. 12a).[83] Both $VO_2 \cdot xH_2O$ and $(NH_4)_2V_{10}O_{25} \cdot 8H_2O$ have tunnel structures (Fig. 12b), while the (001) plane of $(NH_4)_2V_{10}O_{25} \cdot 8H_2O$ has a larger lattice spacing at a smaller angle, which may lead to its structural instability. In SEM, $(NH_4)_2V_{10}O_{25} \cdot 8H_2O$ exhibits a cross-linked and unclear nanobelt structure, while $VO_2 \cdot xH_2O$ exhibits a 10–30 nm nanobelt structure. $VO_2 \cdot xH_2O$ nanobelts possess excellent order and can be interwoven to form a stable nanonetwork structure, which is beneficial for Zn^{2+} transport and storage. According to TG, each VO_2 contains 0.35 grams of crystalline water. These water molecules act as a lubricant, weakening the electrostatic interaction between Zn^{2+} and the active material and enhancing transport. The $VO_2 \cdot xH_2O$ electrode can still store 376 mA h g^{-1} after 200 cycles at 1 A g^{-1}. The $VO_2 \cdot xH_2O$ electrode retained specific capacity after 2000 cycles at 5 A g^{-1} was 289 mA h g^{-1} (Fig. 12c). Fig. 12d depicts full and enlarged colormap 3D waterfall plots with the projection of *in situ* XRD of the $VO_2 \cdot xH_2O$ electrode during the first three cycles. The diffraction peak at $2\theta = 14.4°$ is significantly shifted during discharge due to the insertion of Zn^{2+} and the decrease of electrostatic bond strength, which increases the lattice spacing. During the subsequent charging process, the diffraction peak of $VO_2 \cdot xH_2O$ undergoes the opposite process. The *in situ* XRD test results of the $VO_2 \cdot xH_2O$ electrode show that its zinc storage process is based on

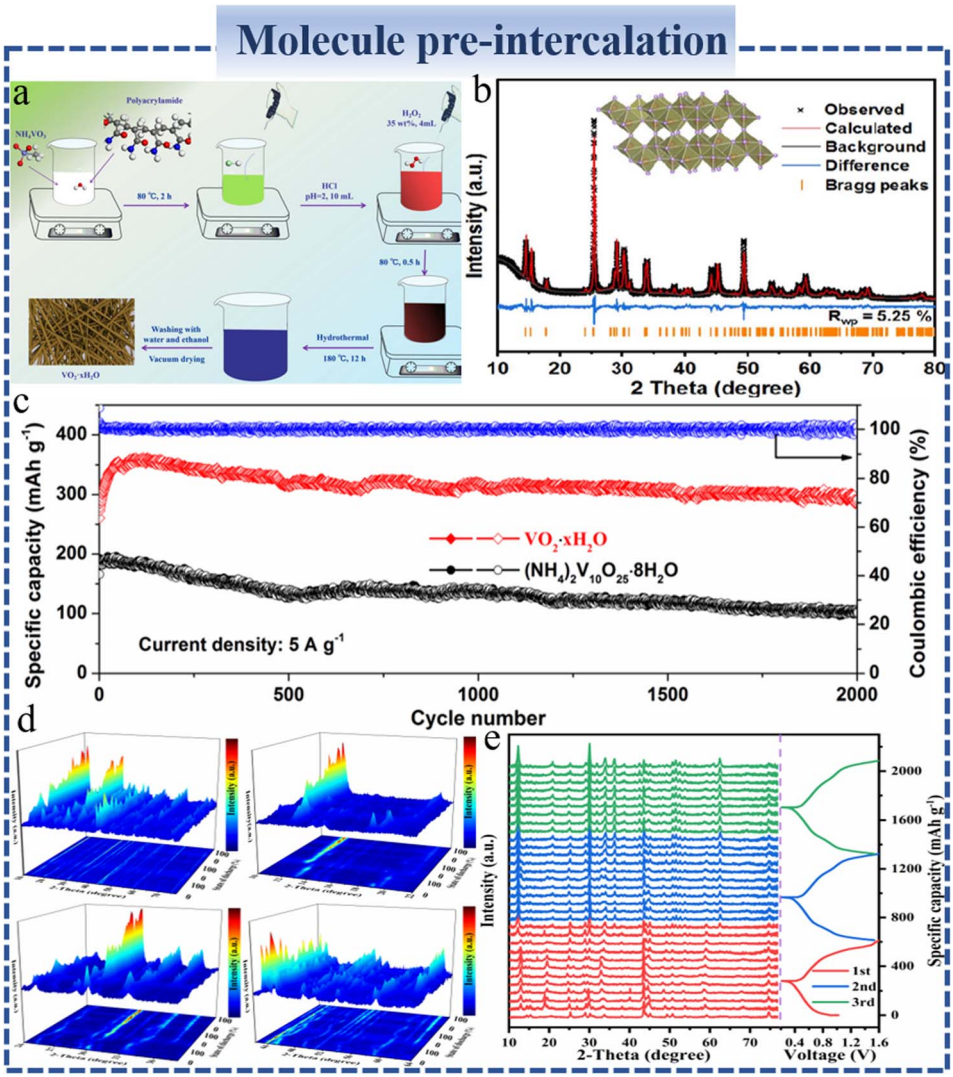

Fig. 12 (a) Schematic diagram of the synthesis of the $VO_2 \cdot xH_2O$ material, (b) XRD pattern of $VO_2 \cdot xH_2O$, (c) long-cycle curve of the $VO_2 \cdot xH_2O$ electrode at a current density of 5 A g^{-1}, (d) the full and enlarged corresponding 3D colormap surface with the *in situ* XRD pattern of the $VO_2 \cdot xH_2O$ electrode, (e) line spectrum from the result of *in situ* XRD of the $VO_2 \cdot xH_2O$ electrode and corresponding discharge/charge curve.[83] Copyright 2022, the Royal Society of Chemistry.

the H^+/Zn^{2+} co-insertion/extraction (Fig. 12e). During the discharge process, H^+ and Zn^{2+} will synergistically embed into the main structure of $VO_2 \cdot xH_2O$, and the increase in OH^- concentration in the electrolyte will lead to the formation of $Zn_x(CF_3SO_3)_y(OH)_{2x-y} \cdot nH_2O$. There are two phases in the charging process that are responsible for the extraction of H^+ and Zn^{2+} from the main structure of $VO_2 \cdot xH_2O$ into the electrolyte, resulting in the decomposition of by-products. The energy storage mechanism revealed that some by-products $Zn_x(CF_3SO_3)_y(OH)_{2x-y} \cdot nH_2O$ were produced during discharge, but the by-products underwent reversible reactions during the cycle.

A vanadium-based oxide containing organic molecules exhibits excellent properties in terms of energy density, structural stability, and conductivity. Ye's group successfully prepared monoclinic VO_2 intercalated with polyaniline (PANI) using a simple hydrothermal method.[84] L-PANI–VO_2 and PANI–VO_2 are the compounds prepared by adding 0.16 and 0.32 mL of hydrochloric acid, respectively. The VO_2 crystal structure can be optimized, with the layered L-PANI–VO_2 exhibiting an interlayer spacing of 10.2 Å. A larger interlayer spacing allows for the embedding of more Zn^{2+} ions. The specific capacity of the L-PANI–VO_2 electrode can reach 415 mA h g^{-1} at 0.1 A g^{-1}. Moreover, the intercalation of the conductive polymer enhances the electronic cloud structure of the material, which improves the diffusion rate of Zn^{2+} ions. This, in turn, boosts the charge/discharge rate performance of the battery. The specific capacity of L-PANI–VO_2 is 415, 380, 365, 340, 320, 290, 270 and 175 mA h g^{-1} at 0.1, 0.2, 0.3, 0.5, 1.0, 2.0, 3.0 and 5.0 A g^{-1}, respectively. The SEM image reveals that L-PANI–VO_2 possesses a layered structure with well-defined edges and a smooth surface. The L-PANI–VO_2 sheets typically measure over ten microns in length and range from 100 to 200 nm in thickness. The CV curve of the L-PANI–VO_2 composite material displays four pairs of redox peaks at 0.35/0.48, 0.55/0.70, 0.92/1.04, and 1.32/1.43 V, which correspond to the insertion and extraction of Zn^{2+} ions. This indicates a multi-step charge storage process at a low scan rate. In contrast, the CV curve of the PANI–VO_2 composite material shows only two pairs of redox peaks. Electrochemical testing further confirms that the L-PANI–VO_2 composite material exhibits a significantly higher specific capacity compared to the PANI–VO_2 composite material, as indicated by the larger peak areas in the cyclic voltammetry curves.

5.3 Composites with other materials

To prevent VO_2 crystals from changing shape and dissolving, they can be coated with carbon-based materials, metal oxides, conductive polymers, *etc.* Long-term cycle stability is achieved by stabilizing the crystals and preventing volume changes caused by ion insertion and extraction during charging and discharge. The abundance of free electrons inside the carbon coating can improve conductivity, which facilitates the fast transfer of electrons. Additionally, in some cases, carbon coatings have been shown to reduce the interfacial resistance between the cathode and the electrolyte, thereby increasing the overall conductivity of the system. By calcining organic matter in a specific atmosphere and retaining a carbon layer after the calcination process, the carbon coating can be obtained.[85–87] For carbon coating, acetylene (C_2H_2) gas with a high carbon content is a good raw material. VO_2 can be calcined in a mixture of C_2H_2 and argon to produce VO_2@C nanobelts with different microstructures (Fig. 13a).[88] As can be seen from the SEM, there is

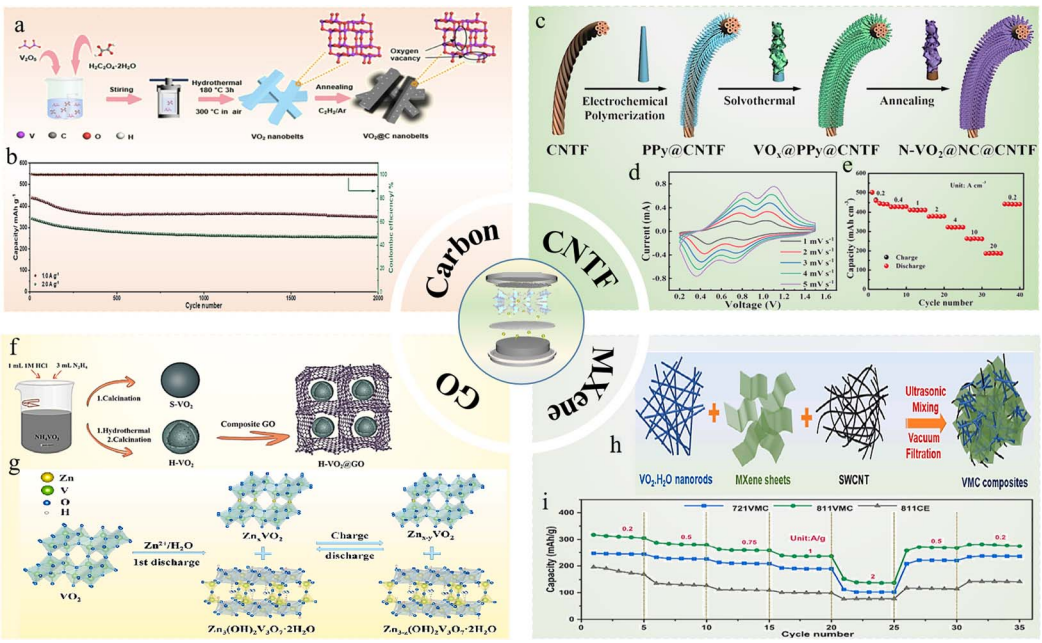

Fig. 13 (a) Synthesis route and structural diagram of VO_2@C and (b) VO_2@C cycle performance diagram.[88] Copyright 2023, the Royal Society of Chemistry. (c) Synthesis route of N–VO_2@NC@CNTF, (d) CV diagrams at different scan rates and (e) rate performance of N–VO_2@NC@CNTF//Zn@CNTF.[90] Copyright 2023, Wiley-VCH. (f) Synthesis route of H–VO_2@GO, and (g) Schematic diagram of the H–VO_2@GO reaction mechanism[92] Copyright 2024, Elsevier. (h) Synthesis diagram of VMC and (i) rate performance of the VMC electrode.[99] Copyright 2024, Elsevier.

a coating layer of about 2 nm on the VO_2 nanobelt. According to further analysis, the coating is a carbon layer, and the crystal structure of VO_2 has not changed significantly. The addition of oxygen vacancies to the AZIBs through carbon coating also increases active sites, contributing to higher electrochemical performance compared to AZIBs with pure oxygen. After low current activation, VO_2@C nanobelts can achieve an initial capacity of 438/342 mA h g^{-1} at 1/2 A g^{-1} (Fig. 13b). Moreover, He's group successfully prepared carbon-coated VO_2 ($H_{1.99}VO$@C) by a hydrothermal reaction of VO_2 with glucose and subsequent annealing.[89] Carbonized carbon is provided by glucose to achieve the coating of rod-shaped VO_2 with a carbonized carbon shell. Carbon shells can improve conductivity and mechanical properties. $H_{1.99}VO$@C electrodes have a specific capacity of 425 mA h g^{-1} at 0.1 A g^{-1}.

Due to their excellent conductivity, carbon nanofibers have been widely used in energy storage devices in recent years. The use of these materials can enhance electron transmission capacity, reduce battery internal resistance, and increase the power density and charging efficiency of batteries. During the charge/discharge process, the volume change of the cathode material can cause stress, which can be relieved with the high strength and toughness of carbon nanofibers, which also prevent the collapse of the cathode material, improving the battery's cycle stability. Carbon nanofibers, in addition to having a high specific surface area, also increase the contact area between the positive electrode material and the electrolyte. Increasing the contact area increases the number of active sites, which increases the capacity and energy density of the battery. N–VO_2@NC@CNTF was obtained after calcination by Guo *et al.*[90] through growing nitrogen-doped vanadium dioxide on carbon nanotube fibers (CNTFs) (Fig. 13c). During calcination, the polypyrrole (PPy) deposited on CNTF releases ammonia, which results in the introduction of N. On CNTFs, densely deposited PPy nanowires are observed. PPy nanowires enhance the conductivity of carbonized nanocomposites and provide conductive scaffolds for regulating the loading of the active materials in the outer layer. Even after calcination, scanning electron microscopy images show that N–VO_2@NC@CNTF retains its structural integrity and the unique characteristics of high porosity and a large specific surface area. They assembled an entangled quasi-solid FAZIB with the N–VO_2@NC@CNTF cathode and Zn@CNTF anode coated with $ZnSO_4$/CMC gel electrolyte. Charge–discharge curves demonstrate the superiority of the NC NW scaffold and N doping, where VO_2@-NC@CNTF//Zn@CNTF is significantly more specific than VO_2@CNTF//Zn@CNTF, and N–VO_2@NC@CNTF//Zn@CNTF is significantly more specific than VO_2. Moreover, the CV curves of the FAZIB at different scan rates clearly show that the curve has two pairs of oxidation and reduction peaks, which are caused by the multi-step insertion/deinsertion mechanism for Zn^{2+} (Fig. 13d). The specific capacity of the FAZIB is 441.383 mA h cm^{-3} at 0.2 A cm^{-3}. This indicates that the FAZIB has excellent rate performance due to its improved conductivity (Fig. 13e). The advantages of carbon nanotubes are also similar. The unique flower-like structure of the VO_2 and CNT composites facilitates the contact between the electrode and electrolyte, thereby reducing the diffusion distance of Zn^{2+}. The VO_2/CNT composites exhibit high reversible capacity (410 mA h g^{-1} at 0.1 A g^{-1}), excellent cycling stability (reversible capacity of 221 mA h g^{-1} after 2000 cycles at 5 A g^{-1}), and good rate capability.[91]

The graphene oxide (GO) material is a novel type of carbon material that exhibits excellent performance. GO contains many oxygen-containing functional groups, including epoxide, carbonyl, carboxyl, and hydroxyl, which can be reduced to obtain reduced graphene oxide (rGO). Although some oxygen-containing functional groups are reduced in graphene, its partial conjugated structure is restored, making it conductive. As rGO can be well compounded with metal oxides, it is added to VO_2 to achieve carbon coating and defect formation. Li *et al.*[92] used a hydrothermal method and high-temperature calcination method to pre-prepare hollow VO_2 microspheres and then composited them with GO to form redox graphene-anchored hollow VO_2 microspheres. The hollow morphology of microspheres provides a large specific surface area and a large number of electrochemical reaction sites, enabling them to store energy efficiently and resist volume stress during Zn^{2+} deintercalation, which greatly enhances their microstructural stability. Additionally, GO enhances the material's conductivity and increases its ion diffusion rate. The 400 nm nanospheres (S–VO_2) exhibit obvious lattice fringes. After calcination, a hollow sphere structure (H–VO_2) is formed, which reduces the crystallinity, providing more active sites for ion storage (Fig. 13f), making it a highly efficient electrochemical material. As a result, the specific discharge capacities of the H–VO_2 electrode are 400.1/261.5 mA h g^{-1} at 0.5/10 A g^{-1}, respectively. *Ex situ* testing was conducted to investigate the energy storage mechanism of the H–VO_2 electrode. $Zn_3(OH)_2V_2O_7 \cdot 2H_2O$ is formed during the charge and discharge process of the first cycle and participates in subsequent energy storage (Fig. 13g). Directly dispersing VO_2(B) powder on rGO sheets can also achieve carbon coating.[93,94] Polystyrene nanospheres and redox graphene nanosheets were also added to the spray solution, and spherical electrode materials were formed by spray pyrolysis. VO_2 nanosheets were anchored in the layers of redox graphene microspheres, resulting in a composite of rGO and vanadium oxide (P–VO_2@rGO). The P–VO_2@rGO electrode can achieve a specific capacity of 342 mA h g^{-1} at 0.1 A g^{-1}.[95] In addition to redox graphene, expanded graphite with good conductivity and stability can also be composited with VO_2.[96]

As an alternative coating material for VO_2, MXene is a 2D transition metal carbide, nitride, or carbonitride that has excellent electrical conductivity, outstanding mechanical properties, and adjustable surface end groups.[97] The most troublesome thing about MXene, however, is the fact that it needs to be pretreated before use.[98] Wang's group successfully used MXene nanosheets as conductive adhesives for anchoring $VO_2 \cdot xH_2O$ nanorods and single-walled carbon nanotubes (SWCNTs) (Fig. 13h).[99] Compared to the traditional method of scraping materials on flexible substrates, this technique provides a flexible and stable electrode by preventing the active material from falling off as happens with traditional scraping electrodes when repeatedly deformed under repeated deformation conditions.

SEM images reveal that VMC consists of interconnected one-dimensional (1D) nanorods, 1D nanotubes, and 2D nanosheets. The microstructure can be revealed through SEM images of VMC cross sections. $VO_2 \cdot xH_2O$ nanorods are preferentially distributed on MXene sheets by van der Waals interactions, forming a hierarchical structure. Additionally, SWCNTs provide mechanical support and flexibility for the cathode, facilitating rapid charge transfer and long-term cycling. In combination with VO_2, this low-dimensional carbon material can improve conductivity and increase active sites, thereby improving electrochemical performance and rate performance (Fig. 13i). The VMC electrode exhibits an ultrafast ion diffusion rate (10^{-10} to 10^{-7} cm^2 s^{-1}). This is mainly due to the unique 3D network structure constructed from MXene sheets, $VO_2 \cdot xH_2O$ nanorods and SWCNTs, which provides an efficient electron transmission path and ion diffusion channel.

In various battery systems, atomic layer deposition (ALD) is one of the most effective methods to solve the interface problems of electrodes because it is one of the most precise coating methods.[100] ALD layers cannot only protect the electrode from adverse side reactions at the interface in order to inhibit cathode dissolution, but can also serve as an artificial cathode electrolyte interface to facilitate the transfer of Zn^{2+} between the electrode and electrolyte. Boruah *et al.*[101] have applied a layer of ZnO to a carbon fiber (CF) current collector as a hole and electron transport layer. Growing VO_2 directly on the ZnO layer improved charge separation and the interface between the active materials, resulting in an increase in light conversion efficiency. Shuai *et al.*[102] inhibited vanadium dissolution and side reactions using an ALD zinc oxide layer (ZnO@VOH) on a hydrated vanadium dioxide nanosheet cathode. The XRD analysis showed that the original crystal structure did not change much after deposition on ZnO. In electrochemical tests, the ZnO@VOH electrode retained 74% to 89% of its capacity after 100 cycles at 0.5 A g^{-1} and 29% to 71% after 990 cycles at 5 A g^{-1}. An XRD analysis of the ZnO@VOH electrode at different cycle numbers revealed a very stable crystal structure, indicating that the material is cycle stable. By comparing the morphology of the ZnO@VOH electrode in the original state and after 20 cycles at 0.2 A g^{-1}, it was found that the morphology of the nanosheets was well preserved, further confirming that the ZnO on the surface protected the vanadium oxide. Moreover, Cheng's group has successfully prepared a material containing a heterojunction structure by a microwave-assisted hydrothermal method, which is composed of bismuth vanadate ($BiVO_4$) and vanadium dioxide (VO_2).[103] Due to the dual-phase structure, the interlayer spacing is enhanced, more pathways are provided for Zn^{2+} transport, and excellent stability is ensured, resulting in outstanding electrochemical performance.

5.4 Defect engineering

By adjusting the electronic structure, increasing active sites, optimizing ion transport paths, and improving structural stability, it is possible to improve the electrochemical performance of electrode materials. Traditional defect engineering includes oxygen defects and vacancy defects, with oxygen defect engineering being widely used in vanadium oxides. Introducing oxygen vacancies into vanadium oxides modifies the electronic structure, band structure, charge distribution, and density of states. This alteration enhances conductivity, boosts activity, and improves energy storage capabilities, while also inhibiting undesirable phase transitions. Unfortunately, defects can alter the reaction kinetics of a material by acting as an active site that promotes or hinders oxidation reactions. They also affect the stability of the material, which can lead to faster degradation and reduced electrochemical performance over time. Therefore, it is important to consider appropriate deficiencies and develop strategies to minimize their adverse effects. Cao's group used multiple phase transition methods to successfully prepare VO_2(B) rich in oxygen vacancies.[104] Due to oxygen defects increasing the active site and improving ion diffusion and transport, the oxidation reaction rate of VO_2 during charging may be increased. This means that in the same amount of time, more VO_2 can be oxidized to higher-priced vanadium ions. As a result, it showed a discharge capacity of 325.6 mA h g^{-1} at 0.05 A g^{-1}, while the capacity retention rate was 86% after 5000 cycles at 3.0 A g^{-1}. As graphene exhibits excellent electrical conductivity, Li *et al.* created oxygen vacancies in VO_2/G nanobelts by attaching vanadium oxide to redox graphene.[105] Incorporating graphene can maintain vanadium oxide's morphology and increase the diffusion rate of Zn^{2+} by accelerating charge transfer. Yuan *et al.* also combined VO_2 with GO through a hydrothermal route to construct a vanadium dioxide/GO composite material rich in oxygen vacancies (VO_2(B)/GO).[106] VO_2(B)/GO showed excellent electrochemical performance (423/227 mA h g^{-1} at 0.5/15 A g^{-1}). The one-step hydrothermal method to *in situ* prepare defective VO_2 is economical and effective in comparison with most methods that synthesize VO_2 first and then introduce defects. Ascorbic acid and V_2O_5 can be hydrothermally treated to produce VO_2 rich in oxygen defects (O_d-VO_2). By adjusting the amount of ascorbic acid, oxygen vacancies can be controlled. O_d-VO_2 presents a layered stacking structure in SEM. The O_d-VO_2 electrode exhibits excellent zinc storage properties (92.6% capacity retention after 2000 cycles at 3.0 A g^{-1}).[107]

Nanostructures provide high surface areas, short ion diffusion paths, and porous structures that facilitate electrolyte diffusion and maintain volume changes during the insertion and extraction of ions. The use of graphene sheet nanocomposites can enhance cycle stability and rate performance at high currents. By weakening the strong interaction between Zn^{2+} and the vanadium oxide skeleton, a lattice defect can enhance zinc ion transport. As a result of the above three optimization strategies, Huang *et al.*[108] were able to fabricate 3D sponge-like hydrated vanadium dioxide composites that contain abundant oxygen vacancy defects and graphene that has been modified by one-step hydrothermal treatment. In Fig. 14a, 2D hydrated vanadium dioxide nanorods with oxygen vacancies are intertwined with rGO nanosheets to form a nanowall (O_d-HVO/rG). The rGO nanosheets cover a large number of hydrated vanadium dioxide nanorods with oxygen vacancies, preventing them from stacking. Due to their 3D

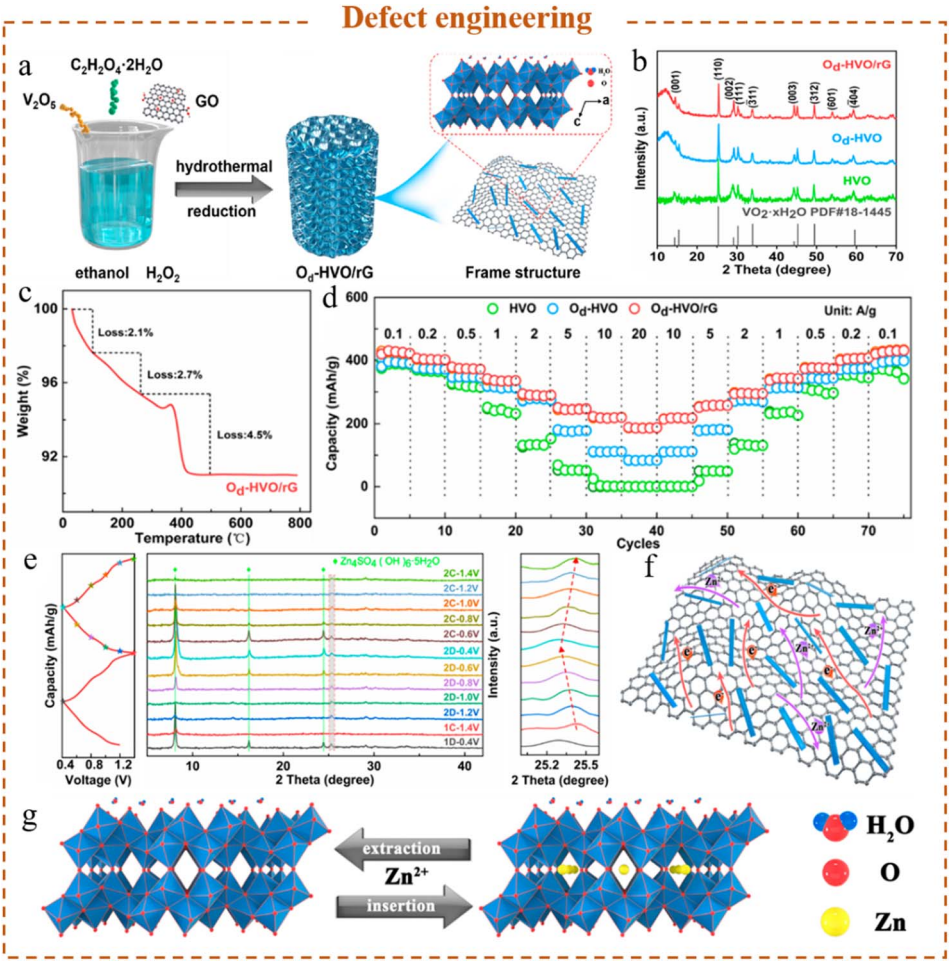

Fig. 14 (a) Schematic diagram of the synthesis of O_d-HVO/rG materials, (b) XRD patterns of all samples, (c) TGA curve of O_d-HVO/rG, (d) rate performance of HVO, O_d-HVO and O_d-HVO/rG, (e) *ex situ* XRD of O_d-HVO/rG, and (f and g) schematic diagram of the energy storage mechanism of O_d-HVO/rG.[108] Copyright 2021, American Chemical Society.

structure, sponges are less susceptible to structural collapse and damage during electrochemical reactions. The XRD spectra of HVO, O_d-HVO, and O_d-HVO/rG are consistent with those of $VO_2·xH_2O$. O_d-HVO and O_d-HVO/rG show weaker intensities than HVO, indicating that oxygen vacancy defects have decreased the crystallinity of O_d-HVO and O_d-HVO/rG. The thermogravimetric analysis in Fig. 14c indicates that a 2.1% weight loss occurs when adsorbent water evaporates at 100 °C; when the temperature is between 100 °C and 500 °C, it is 2.7% of the crystal structure water loss, and 4.5% of the weight loss, which can be converted to 11.8% for reduced graphene. In addition to increasing capacity, oxygen vacancies in the O_d-HVO/rG electrode can reduce electrostatic interactions between Zn^{2+} and the host material. rGO enhances conductivity, suppresses crystal distortion, and achieves high stability in the O_d-HVO/rG electrode. O_d-HVO/rG electrodes exhibit a high initial charge capacity of 428.6 mA h g^{-1} at 0.1 A g^{-1} (Fig. 14d). The energy density and power density of O_d-HVO/rG are compared with those of other reported cathodes in Fig. 14c. O_d-HVO/rG exhibits a superior energy density (245.3 W h kg^{-1}) and power density (71 W kg^{-1}). To clarify the reaction mechanism and structural evolution of the O_d-HVO/rG electrode during cycling, an *ex situ* XRD analysis was performed (Fig. 14e). A number of obvious characteristic peaks were observed during the discharge process of the O_d-HVO/rG electrode at 8.1°, 16.2°, 24.4° and 29.3°, which can be attributed to the characteristic peak of $Zn_4SO_4(OH)_6·5H_2O$. After charging at 0.4–1.4 V, $Zn_4SO_4(OH)_6·5H_2O$ gradually disappeared, indicating that $Zn_4SO_4(OH)_6·5H_2O$ was reversibly and continuously generated and decomposed. The embedding and spacing reduction of Zn^{2+} during the discharge process resulted in a noticeable diffraction peak shift on the (110) crystal plane of O_d-HVO/rG. As a result of charging, the diffraction peak returned to its original position, indicating that Zn^{2+} had been removed. O_d-HVO/rG contains continuously precipitated H^+ and Zn^{2+}, as well as OH^- that is formed when water decomposes (Fig. 14f and g). A special atmosphere can also be used to produce oxygen vacancies in defect engineering by calcining vanadium oxides with special substances. To create oxygen vacancies, Liu *et al.*[109] used a hydrothermal method to grow VO_2 nanorods on polydopamine-coated gourd-shaped carbon and then calcined them with sodium borohydride under an argon atmosphere.

The uniform gourd carbon matrix can enhance electronic conductivity by supplying additional Zn^{2+} storage sites and weakening the electrostatic interaction between Zn^{2+} and VO_2.

5.5 Elemental doping

Different from ion pre-intercalation, elemental doping here mainly refers to the doping of mostly non-metallic elements and a small proportion of metallic elements. These non-metallic elements replace the original position of oxygen, which not only changes the electronic structure and spatial configuration of the crystal, but also accelerates electron/ion dynamics, thereby playing a crucial role in improving the material. Metal doping replaces the original position of V, increases the lattice parameters of the material, enhances its thermal and chemical stability, and thus extends the service life of the battery. In AZIBs, the low conductivity of VO_2(B) and the slow migration rate of Zn^{2+} hinder its application. The crystal structure and electrochemical performance of vanadium oxide can be improved by nitrogen doping. By calcining tunnel-type VO_2(B) in an ammonia atmosphere, Gu *et al.* prepared nitrogen-doped VO_2 (Fig. 15a).[110] Heat treatment at different temperatures in NH_3 preserved the VO_2 nanobelt structure well. As the calcination temperature increased, the edges of the VO_2 nanobelts gradually melted and aggregated. As a result of high-temperature reactions, nanobelt aggregates were also confirmed by TEM. The HRTEM images of the material (VO_2–N400) at 400 °C revealed lattice fringes with a spacing of 0.353 nm, which corresponds to the (110) plane of VO_2(B). The lattice of nitrogen atom incorporation also exhibited a variety of disordered structural regions. VO_2–N400 exhibits excellent rate performance and cycle stability due to the introduction of N (Fig. 15b). Structural and electrochemical characterization studies have demonstrated that the introduction of N into VO_2(B) results in lattice expansion, grain size reduction, and partial structural disorder. The electrochemical performance of VO_2(B) in AZIBs is superior to that of this product due to its fast ion transport, additional ion storage sites, and inhibition of structural degradation. The VO_2–N400 electrode has a specific capacity of 373.7 mA h g^{-1} at 0.1 A g^{-1} (Fig. 15c). *Ex situ* XRD characterization was conducted to determine how Zn^{2+} ions are stored in VO_2–N400. The *ex situ* XRD pattern of the VO_2–N400 electrode in the first cycle revealed four monoclinic VO_2(B) peaks at 25.2°, 30.0°, 35.8°, and 44.9°. These peaks suggest that VO_2–N400 has good reversibility and structural stability for the storage of Zn^{2+}. In addition, a new phase, $Zn_2(OH)_2V_2O_{5.72}N_{1.28}\cdot 2H_2O$ (12.4° and 22.7°), was detected, which appeared with the insertion of Zn^{2+} and disappeared with the extraction of Zn^{2+}, indicating that the zinc storage process is based on the H^+/Zn^{2+} co-insertion/extraction.

As opposed to nitrogen doping, metal atoms (such as tungsten, molybdenum, and niobium) can be introduced into the center of the lattice polyhedron to replace vanadium atoms, thus improving the crystal structure and performance.[111] A hydrothermal method was used by Li *et al.*[112] to dope tungsten (W) into VO_2 crystals. Using tungstic acid (H_2WO_4) and ethylene glycol, ammonium metavanadate (NH_4VO_3) was first

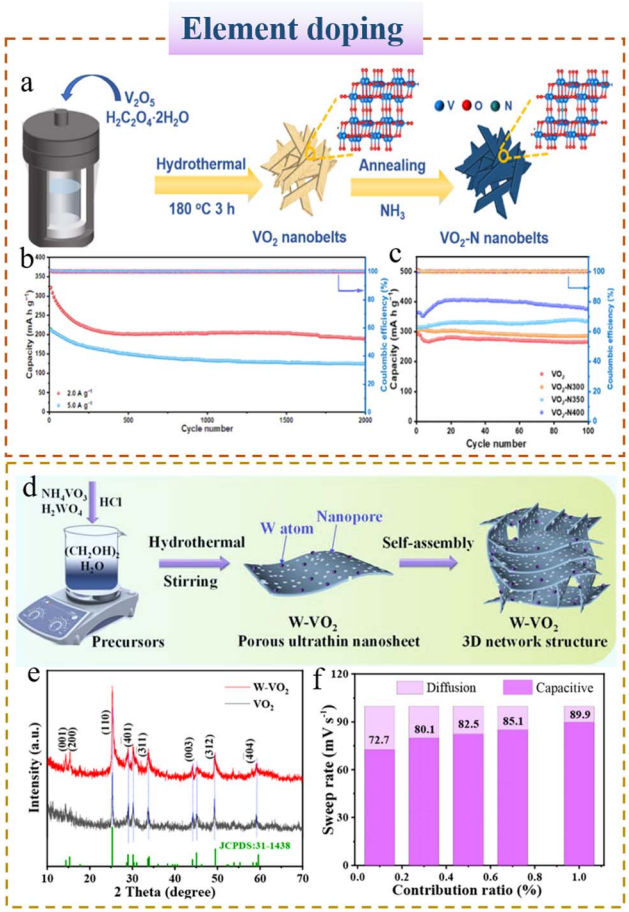

Fig. 15 (a) Schematic diagram of the synthesis of VO_2–N nanobelts, (b) long cycle performance curves of VO_2–N400 at 2/5 A g^{-1}, and (c) cycle performance curves of VO_2–N with different calcination temperatures at 0.1 A g^{-1}.[110] Copyright 2023, Elsevier. (d) Schematic diagram of the synthesis of W–VO_2, (e) XRD patterns of VO_2 and W–VO_2, and (f) contribution ratio between capacitance and diffusion-controlled capacitance.[112] Copyright 2021, American Chemical Society.

decomposed to form V_2O_5 nanoparticles, which were then self-assembled into a three-dimensional network structure (W–VO_2). W–VO_2 content was controlled by the concentration of tungstic acid in the precursor solution. Ultrathin nanosheets of W–VO_2 were observed. The thickness of W–VO_2 was significantly lower than that of pure VO_2 (nanoparticles). On the ultrathin nanosheets of W–VO_2, mesopores can be seen due to the introduction of tungsten atoms and the generation of a large amount of gases (such as NH_3 and CO_2). The XRD pattern of W–VO_2 shows that W doping does not alter the VO_2 crystal phase diagram (Fig. 15e). Interestingly, the addition of W does not cause a significant shift in the diffraction peak but rather increases its intensity, which is explained by the low W doping content of W–VO_2, which does not cause a noticeable shift. However, introducing W leads to stronger V–O bond stretching vibration, so the intensity increases. When W–VO_2 is tested in the voltage range of 0.2–1.4 V, an incomplete CV curve can be seen during the first cycle, which may be attributed to the

relatively low open circuit voltage. The pseudocapacitive effect becomes more obvious as the scan rate increases, indicating that the electrochemical behavior of the W–VO_2 electrode is primarily influenced by the pseudocapacitive effect (Fig. 15f). In W–VO_2, the stronger W–O bond results in a weaker electrostatic interaction between zinc and oxygen, which is why W–VO_2 is the preferred positive electrode for AZIBs because of its superior zinc storage performance. At 0.1 A g^{-1}, W–VO_2 has an initial reversible capacity of 346 mA h g^{-1}; it retains 281.3 mA h g^{-1} after 100 cycles. To investigate the zinc storage mechanism in W–VO_2, *ex situ* XRD and XPS characterization studies were conducted. In the *ex situ* XRD pattern, the peak at 25.6° shifted slightly downwards, corresponding to the expansion in the distance between VO_2 interlayers during discharge, which could be explained by the embedding of zinc atoms, which resulted in a decrease in the distance between W and VO_2. As shown by the *ex situ* XPS spectrum of V 2p, the peak changes of V^{4+} and V^{3+} are consistent, indicating the stability of the cycle.

The material structure can be intrinsically adjusted through doping strategies in order to enhance performance. The dopant atoms are not introduced into the center position of the lattice polyhedron. Incorporating dopant atoms into the gaps of the lattice polyhedron can increase tunnel size and stabilize the lattice at the same time. The element boron (B) usually exists as B^{3+}, which is small and low in atomic weight, so using B element for interstitial doping makes sense.[113] Through the use of H_3BO_4 as a precursor, an interstitial boron-doped tunnel-type VO_2(B) was successfully prepared by a hydrothermal method. The XRD spectrum of boron-doped VO_2(B) shifts to the left because of the interstitial doping of boron. The lattice spacing of the (110) plane of the boron-doped product increases to 0.012 nm as boron occupies the interstitial position and forms boron–oxygen bonds, which cause oxygen atoms to shrink and the lattice spacing to increase. The specific capacity of boron-doped VO_2(B) is 281.7 mA h g^{-1} at 0.1 A g^{-1}. The tunnel-type VO_2(B) retains a capacity of 133.3 mA h g^{-1} after 1000 cycles at 5 A g^{-1}, indicating that interstitial boron doping can improve its Zn^{2+} storage capacity. To verify the universality of boron doping, different concentrations of boron were added to tunnel-type MnO_2. It is interesting to note that boron doping is universally used to increase zinc storage capacity in manganese-based products.

6. Conclusion and practical prospects

Recent research on VO_2-based cathode materials for AZIBs has shown remarkable progress. When the zinc anode and electrolyte are optimized to match each other, this battery system could serve as a promising candidate for large-scale applications. However, like all metal oxide cathode materials, VO_2 still faces significant challenges such as dissolution, byproduct formation, and slow diffusion rates, which hinder its widespread use. Various modification strategies have been employed to enhance the electrochemical performance of AZIBs, including ion intercalation, molecular intercalation, composite materials, and defect engineering. Ion intercalation stabilizes the cathode's structure and improves its kinetics, while molecular intercalation enhances the overall conductivity and further stabilizes the crystal structure. The use of composite materials can help prevent the collapse of the cathode structure, improving both conductivity and electrochemical properties. Moreover, composite materials offer a new avenue for developing more effective cathode materials. Defect engineering plays a critical role in enhancing the structural stability and electrochemical performance of VO_2-based cathodes. By introducing or controlling defects, it is possible to modify the crystal structure of the material to improve its properties. Additionally, elemental doping can optimize electrochemical performance by tuning the energy band structure and enhancing the ion diffusion rate, achieved by incorporating foreign elements into the VO_2 crystal lattice.

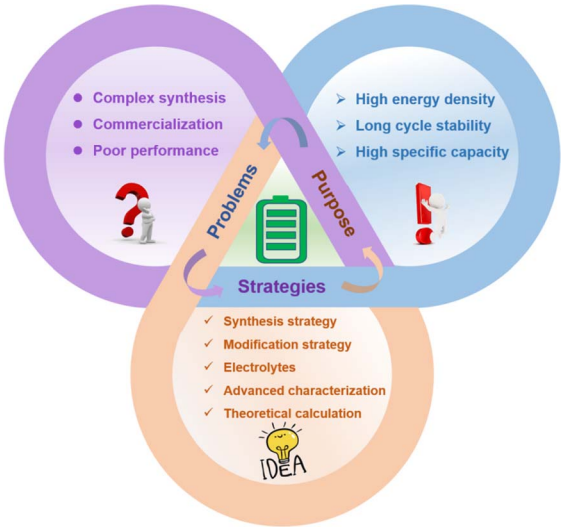

Fig. 16 Schematic diagram of the strategy for the application of VO_2-based cathodes in AZIBs.

VO_2, as a cathode material for AZIBs, necessitates comprehensive research and innovation from various perspectives to reach commercialization and further broaden its application potential. This review highlights key areas for future exploration, including the innovation of synthesis methods, enhancement of optimization strategies, refinement of electrolytes, and the development of advanced characterization techniques (Fig. 16).

6.1 In-depth exploration of the VO_2 synthesis strategy

Currently, VO_2 is mainly synthesized through redox reactions starting from V_2O_5. However, it must be noted that this traditional method may suffer from several disadvantages such as high energy consumption, low yield, or insufficient purity of the final product. As a consequence, to improve the performance of VO_2 and reduce the cost of VO_2, it is crucial to explore new synthesis routes. Due to their unique structure and properties, metal–organic frameworks (MOFs) provide new ideas for synthesizing VO_2 with their unique structure and properties as a new type of compound. The characteristics of MOFs are that they have a large specific surface area, high porosity, diverse

structural tunability, and excellent versatility. The MOF derivatives obtained through calcination can maintain the structural advantages of the original MOFs. In addition to controlling the morphology and size of VO_2 using MOF precursors or templates, it is also possible to introduce new properties or functions into VO_2 using MOFs as precursors or templates. By adjusting the structure and composition of MOFs, it is possible, for example, to dope or composite VO_2 to improve its electrochemical efficiency.

6.2 Multi-strategy collaborative optimization

To improve one aspect of performance, a single modification often comes at the expense of another. It is necessary to integrate multiple optimization measures to achieve a high-performance VO_2-based cathode. By carefully regulating the crystal structure, morphology, and size of VO_2, its ion transmission path and charge storage capacity can be significantly improved. Modification methods such as ion intercalation and carbon coating can also be used to enhance the electrochemical activity, structural stability, and cycle stability of VO_2. Ion intercalation can increase the interlayer spacing by introducing specific ions into the crystal structure of VO_2, thereby providing a greater channel for the insertion and extraction of zinc ions. This results in a reduction in the resistance to ion transmission and an increase in the rate of charging and discharging and the energy density of the battery. To improve the overall conductivity of the material, we can use carbon coatings to create a layer of carbon on the surface of VO_2 particles. By doing so, we are able to extend the life cycle of the battery by preventing the VO_2 structure from being damaged during charging and discharging processes. It is through this technique that AZIBs can be developed with higher storage capacities and longer cycle lives, both of which can contribute greatly to the rapid advancement of AZIB technology in practical applications.

6.3 Improvement of electrolyte adaptation

In AZIBs, the electrolyte plays a crucial role in the performance and stability of the battery. Aqueous electrolyte is another important factor affecting the reversibility of the zinc anode within a specific electrochemical working window. Additionally, aqueous electrolyte controls the dissolution and transfer kinetics of cathode materials. AZIBs' performance can be improved by optimizing the electrolyte. The most commonly studied zinc salts are zinc sulfate ($ZnSO_4$), zinc chloride ($ZnCl_2$), and zinc trifluoromethanesulfonate ($Zn(OTF)_2$). Generally, research focuses more on the type of salt used, but ignores the effect of the amount. From the perspective of energy density, the less electrolyte used, the higher the energy density. As a result of the continuous electrolyte consumption caused by self-corrosion inside the battery, it is necessary to maintain an appropriate amount of electrolyte to maintain normal operation of the battery. Electrolytes must precisely match cathode and anode requirements. Zinc ions must be transported quickly and smoothly in the electrolyte by choosing an electrolyte with high ionic conductivity and low viscosity. To prevent decomposition or performance degradation during battery charging and discharging, the solvent and salt components in the electrolyte need to be chemically and thermally stable. A variety of strategies can be adopted to further optimize the electrolyte's performance. Adding the right amount of additives, such as surfactants or corrosion inhibitors, can improve the stability of the electrolyte and its compatibility with electrode materials. The pH value of the electrolyte is also an important optimization method for improving the electrolyte's overall performance. This new electrolyte system can achieve a balance between a wider working window, better compatibility between positive and negative electrodes, and better safety performance by using dual solvents or even ternary solvents. Choosing this option not only improves the overall performance, but also guarantees a more stable battery system operation.

6.4 Advanced characterization methods and theoretical calculations

In the process of studying VO_2 as a cathode material for AZIBs, advanced characterization methods (*in situ* Raman, synchrotron radiation, scanning tunneling microscopy, *etc.*) can be used to gain a deeper understanding of its performance and structure. During electrochemical reactions, *in situ* Raman can monitor the structural changes in materials in real time, which is crucial for understanding phase change and structural evolution. The *in situ* Raman method reveals the energy storage mechanism of VO_2 materials during the charge and discharge process. Synchrotron radiation light sources can provide deep insights into the microstructural characteristics and evolution mechanisms of VO_2 positive electrode materials. Synchrotron radiation technology can track the dynamic evolution of the material structure and provide direct evidence for understanding VO_2's structural changes during charging and discharge. For understanding the electrochemical properties of VO_2, scanning tunneling microscopy (STM) can be used to study its atomic arrangement and electronic structure. By utilizing this information, researchers can develop cathode materials with higher energy density and better cycle stability. Theoretical calculations, as well as simulations and predictions, can provide a deeper understanding of the advantages and disadvantages of VO_2 cathode materials. For example, first-principles calculations can predict the electronic structure and energy band structure of VO_2. Besides providing theoretical support for experiments, DFT can also simulate the structural changes of VO_2 during charging and discharging.

The exploration of VO_2 as a cathode material for AZIBs presents both challenges and opportunities. Every stage of the process, from synthesis strategies to the enhancement of modification techniques and the adaptation and optimization of electrolytes, is essential and demands continuous innovation and breakthroughs. With deeper research, more efficient and cost-effective methods for synthesizing VO_2 are likely to emerge. Furthermore, applying various modification strategies can improve its electrochemical properties, leading to higher and more stable performance. Additionally, the electrolyte, being a critical component of the battery system, must also be optimized. Enhancing AZIB technology by developing a more

adaptable and efficient electrolyte system will be key. VO_2-based AZIBs hold great potential in energy storage and are poised to make significant contributions to sustainable development.

Data availability

No primary research results, software or code have been included and no new data were generated or analysed as part of this review.

Author contributions

Botao Wan: data curation, writing – original draft. Yajiang Wang: investigation, writing – original draft. Xiudong Chen: conceptualization, project administration, funding acquisition, writing – review & editing. Changchao Zhan: supervision, formal analysis. Huixiong Jiang: conceptualization, supervision. Jin-Hang Liu: investigation, formal analysis. Yun Gao: formal analysis, project administration. Xiaoduo Jiang: resources, formal analysis. Xiaohua Cao: supervision. Hang Zhang: data curation, formal analysis, project administration. Shi-Xue Dou: conceptualization, supervision. Yao Xiao: supervision, visualization, formal analysis, writing – review & editing.

Conflicts of interest

There are no conflicts to declare.

Acknowledgements

This work was supported by the National Natural Science Foundation of China (22163003 and 52402213), the Jiangxi Province Double Thousand Plan (jxsq2023201091), the Jiangxi Provincial Natural Science Foundation (20224BAB214019, 20232BAB204024, and 20232BAB203024), the Science and Technology Project of Jiangxi Provincial Department of Education (GJJ2401837), the Jiujiang Science and Technology Project (S2024QNZZ0008), and the Basic Research Project of Wenzhou City (2024G0197 and 2024G0195).

References

1 X. Chen, X. Yin, J. Aslam, W. Sun and Y. Wang, *Electrochem. Energy Rev.*, 2022, **5**, 12.
2 A. Song, Z. Dan, S. Zheng and Y. Zhou, *Nat. Commun.*, 2024, **15**, 5905.
3 J. Li, M. Luo, K. Wang, G. Li and G. Zhang, *Carbon neutraliz.*, 2023, **2**, 574–584.
4 X. Chen, J. Liu, H. Jiang, C. Zhan, Y. Gao, J. Li, H. Zhang, X. Cao, S. Dou and Y. Xiao, *Energy Storage Mater.*, 2024, **65**, 103168.
5 H. Qi, A. Xie and R. Zuo, *Energy Storage Mater.*, 2022, **45**, 541–567.
6 Y. Chen, X. Hu, X. Chen, J. Liu, Y. Huang and D. Cao, *Chem. Eng. J.*, 2023, **478**, 147411.
7 X. Chen, C. Ci, W. Sun, S. Chen, H. Liu and Y. Wang, *J. Mater. Chem. A*, 2022, **10**, 21701–21715.
8 X. Li, Z. Yu, C. Zhang, B. Li, X. Wu, Y. Liu and Z. Zhu, *Small Methods*, 2024, e2400683.
9 X. Chen, H. Zhang, Y. Gao, J. Liu, X. Cao, C. Zhan, S. Wang, J. Wang, S. Dou and D. Cao, *Carbon neutraliz.*, 2022, **1**, 159–188.
10 A. N. Banerjee and S. W. Joo, *Nanotechnology*, 2024, **35**, 47.
11 P. Cicconi and P. Kumar, *J. Energy Storage*, 2023, **73**, 109197.
12 K. Dhanabalan, K. Aruchamy, G. Sriram, T. Sadhasivam and T. H. Oh, *J. Ind. Eng. Chem.*, 2024, **139**, 111–124.
13 X. Chen, H. Zhang, P. Yan, B. Liu, X. Cao, C. Zhan, Y. Wang and J. Liu, *RSC Adv.*, 2022, **12**, 11484–11491.
14 X. Chen, H. Zhang, P. Yan, X. Cao, C. Zhan and J. Liu, *J. Solid State Chem.*, 2022, **314**, 123430.
15 A. V. Cresce and K. Xu, *Carbon Energy*, 2021, **3**, 721–751.
16 X. Feng, M. Ouyang, X. Liu, L. Lu, Y. Xia and X. He, *Energy Storage Mater.*, 2018, **10**, 246–267.
17 C. F. J. Francis, I. L. Kyratzis and A. S. Best, *Adv. Mater.*, 2020, **32**, e1904205.
18 X. Chen, J. Jian, P. Yan, P. Liu, X. Cao and J. Liu, *Chin. J. Inorg. Chem.*, 2022, **38**, 1752–1758.
19 W. Guo, W. Wei, H. Zhu, Y. Hu, H. Jiang and C. Li, *eScience*, 2023, **3**, 100082.
20 M. T. F. Rodrigues, G. Babu, H. Gullapalli, K. Kalaga, F. N. Sayed, K. Kato, J. Joyner and P. M. Ajayan, *Nat. Energy*, 2017, **2**, 17108.
21 Z. Yang, X. Chen, P. Yan, C. Zhan, Y. Wang and J. Liu, *Ionics*, 2022, **28**, 4149–4158.
22 M. Zheng, H. Tang, Q. Hu, S. Zheng, L. Li, J. Xu and H. Pang, *Adv. Funct. Mater.*, 2018, **28**, 1707500.
23 R. G. Fedorov, S. Maletti, C. Heubner, A. Michaelis and Y. Ein-Eli, *Adv. Energy Mater.*, 2021, **11**, 2101173.
24 X. Chen, W. Sun and Y. Wang, *ChemElectroChem*, 2020, **7**, 3905–3926.
25 H. Zhang, Z. Zeng, S. Cheng and J. Xie, *eScience*, 2024, **4**, 100265–116389.
26 Y. Wu, Z. Zhao, X. Hao, R. Xu, L. Li, D. Lv, X. Huang, Q. Zhao, Y. Xu and Y. Wu, *Carbon neutraliz.*, 2023, **2**, 551–842.
27 J. Lv, B. Wang, J. Hao, H. Ding, L. Fan, R. Tao, H. Yang, J. Zhou and B. Lu, *eScience*, 2023, **3**, 100081.
28 J. Chen, G. Adit, L. Li, Y. Zhang, D. Chua and P. S. Lee, *Energy Environ. Mater.*, 2023, **6**, e12633.
29 Z. Zhang, M. Song, C. Si, W. Cui and Y. Wang, *eScience*, 2023, **3**, 100070.
30 S. K. Das, S. Mahapatra and H. Lahan, *J. Mater. Chem. A*, 2017, **5**, 6347–6367.
31 Y. Hu, P. Wang, M. Li, Z. Liu, S. Liang and G. Fang, *Energy Environ. Sci.*, 2024, **17**, 8078–8093.
32 H. Zhang, F. Ning, Y. Guo, S. Subhan, X. Liu, S. Shi, S. Lu, Y. Xia and J. Yi, *ACS Energy Lett.*, 2024, **9**, 4761.
33 D. Bin, F. Wang, A. G. Tamirat, L. Suo, Y. Wang, C. Wang and Y. Xia, *Adv. Energy Mater.*, 2018, **8**, 1703008.
34 X. Zeng, Z. Gong, C. Wang, P. J. Cullen and Z. X. Pei, *Adv. Energy Mater.*, 2024, **14**, 2401704.
35 D. Yuan, J. Zhao, W. Manalastas, S. Kumar and M. Srinivasan, *Nano Mater Sci.*, 2020, **2**, 248–263.

36 Q. Ni, B. Kim, C. Wu and K. Kang, *Adv. Mater.*, 2022, **34**, e2108206.
37 L. Fan, Y. Ru, H. Xue, H. Pang and Q. Xu, *Adv. Sustain. Sys.*, 2020, **4**, 2000178.
38 C. Qiu, H. Huang, M. Yang, L. Xue, X. Zhu, Y. Zhao, M. Ni, T. Chen and H. Xia, *Energy Storage Mater.*, 2024, **72**, 103736.
39 J. Wang, L. Szabo, D. Madhav, I. Ferreira and V. Vandeginste, *Energy Storage Mater.*, 2023, **63**, 103015.
40 N. Zhang, J. Wang, Y. Guo, P. Wang, Y. Zhu and T. Yi, *Coord. Chem. Rev.*, 2023, **479**, 215009.
41 C. Guo, S. Yi, R. Si, B. Xi, X. An, J. Liu, J. Li and S. Xiong, *Adv. Energy Mater.*, 2022, **12**, 2202039.
42 J. Peng, W. Zhang, Q. Liu, J. Wang, S. Chou, H. Liu and S. Dou, *Adv. Mater.*, 2022, **34**, e2108384.
43 G. Li, L. Sun, S. Zhang, C. Zhang, H. Jin, K. Davey, G. Liang, S. Liu, J. Mao and Z. Guo, *Adv. Funct. Mater.*, 2024, **34**, 2301291.
44 X. Deng, J. Sarpong, G. Zhang, J. Hao, X. Zhao, L. Li, H. Li, C. Han and B. Li, *InfoMat*, 2023, **5**, e12382.
45 G. Song, Y. Shi, S. Jiang and H. Pang, *Adv. Funct. Mater.*, 2023, **33**, 2303121.
46 Y. Dai, C. Zhang, J. Li, X. Gao, P. Hu, C. Ye, H. He, J. Zhu, W. Zhang, R. Chen, W. Zong, F. Guo, I. P. Parkin, D. J. L. Brett, P. R. Shearing, L. Mai and G. He, *Adv. Mater.*, 2024, **36**, 2310645.
47 L. Kou, Y. Wang, J. Song, T. Ai, W. Li, P. Wattanapaphawong and K. Kajiyoshi, *Green Chem.*, 2024, **26**, 1709–1724.
48 M. Chen, S. Zhang, Z. Zou, S. Zhong, W. Ling, J. Geng, F. Liang, X. Peng, Y. Gao and F. Yu, *Rare Met.*, 2023, **42**, 2868–2905.
49 T. Yi, L. Qiu, J. Qu, H. Liu, J. Zhang and Y. Zhu, *Chem. Rev.*, 2021, **446**, 214124.
50 Z. Shao, X. Cao, H. Luo and P. Jin, *NPG Asia Mater.*, 2018, **10**, 581–605.
51 Y. Liu, T. Lv, H. Wang, X. Guo, C. Liu and H. Pang, *Chem. Eng. J.*, 2021, **417**, 128408.
52 Z. Khan, P. Singh, S. A. Ansari, S. R. Manippady, A. Jaiswal and M. Saxena, *Small*, 2021, **17**, 2006651.
53 I. P. Pinnock, Y. Fan, Y. Zhu, B. Narayan, T. Wang, I. P. Parkin and B. B. Deka, *J. Mater. Chem. A*, 2025, **13**, 1372–1383.
54 L. Zhang, L. Miao, B. Zhang, J. Wang, J. Liu, Q. Tan, H. Wan and J. Jiang, *J. Mater. Chem. A.*, 2020, **8**, 1731–1740.
55 X. Zhao, J. Sun, Z. Guo, J. Su, T. Liu, R. Hu, W. Yao and X. Jiang, *J. Mater. Chem. A*, 2022, **446**, 137308.
56 L. Zhang, L. Miao, B. Zhang, J. Wang, J. Liu, Q. Tan, H. Wan and J. Jiang, *J. Mater. Chem. A*, 2020, **8**, 1731–1740.
57 T. Wei, Q. Li, G. Yang and C. Wang, *J. Mater. Chem. A*, 2018, **6**, 8006–8012.
58 J. B. Goodenough, *J. Solid State Chem.*, 1971, **3**, 490–500.
59 B. Aydogdu, S. Aydin, S. P. Sasikala, H. E. Unalan, S. O. Kim and R. Yuksel, *J. Energy Storage*, 2024, **86**, 111264.
60 L. Chen, Z. Yang and Y. Huang, *Nanoscale*, 2019, **11**, 13032–13039.
61 C. Liu, W. Xu, C. Mei, M. Li, W. Chen, S. Hong, W. Y. Kim, S. Y. Lee and Q. Wu, *Adv. Energy Mater.*, 2021, **11**, 2003902.
62 W. G. Kidanu, J. Hur, H. W. Choi, M. I. Kim and I. T. Kim, *J. Power Sources*, 2022, **523**, 231060.
63 F. Han, J. Luo, R. Pan, J. Wu, J. Guo, Y. Wang, Y. Wang, M. Liu, Z. Wang and D. Zhou, *ACS Appl. Mater. Interfaces*, 2022, **14**, 41577–41587.
64 Z. Cao, L. Wang, H. Zhang, X. Zhang, J. Liao, J. Dong, J. Shi, P. Zhuang, Y. Cao, M. Ye, J. Shen and P. Ajayan, *Adv. Funct. Mater.*, 2020, **30**, 2000472.
65 M. Bai, Z. He, J. Hou, J. Gao, L. Kong and J. Alloy, *Compounds*, 2023, **936**, 168218.
66 M. Bai, J. Gao, Z. He, J. Hou and L. Kong, *J. Electroanal. Chem.*, 2022, **907**, 116039.
67 W. Deng, Z. Xu, G. Li and X. Wang, *Small*, 2023, **19**, e2207754.
68 Q. He, T. Hu, Q. Wu, C. Wang, X. Han, Z. Chen, Y. Zhu, J. Chen, Y. Zhang, L. Shi, X. Wang, Y. Ma and J. Zhao, *Adv. Mater.*, 2024, **36**, e2400888.
69 L. Chen, Y. Ruan, G. Zhang, Q. Wei, Y. Jiang, T. Xiong, P. He, W. Yang, M. Yan, Q. An and L. Mai, *Chem. Mater.*, 2019, **31**, 699–706.
70 J. Ding, Z. Du, L. Gu, B. Li, L. Wang, S. Wang, Y. Gong and S. Yang, *Adv. Mater.*, 2018, **30**, e1800762.
71 F. Wan, L. Zhang, X. Dai, X. Wang, Z. Niu and J. Chen, *Nat. Commun.*, 2018, **9**, 1656.
72 Z. Zhang, B. Xi, X. Wang, X. Ma, W. Chen, J. Feng and S. Xiong, *Adv. Funct. Mater.*, 2021, **31**, 2103070.
73 T. Wei, Q. Li, G. Yang and C. Wang, *J. Mater. Chem. A*, 2018, **6**, 8006–8012.
74 J. Ding, H. Gao, K. Zhao, H. Zheng, H. Zhang, L. Han, S. Wang, S. Wu, S. Fang and F. Cheng, *J. Power Sources*, 2021, **487**, 229369.
75 Y. Li, D. Zhang, S. Huang and H. Yang, *Nano Energy*, 2021, **85**, 105969.
76 Y. Li, J. Chen, L. Su, X. Zhang, Q. Zheng, Y. Huo and D. Lin, *J. Colloid Interface Sci.*, 2023, **652**, 440–448.
77 Z. Wang, P. Cui, X. Wang, M. Chang, Y. Yu, J. You, F. Hu, Y. Wu and K. Zhu, *Adv. Funct. Mater.*, 2024, 2407925.
78 Q. Li, X. Ye, Y. Jiang, E. Ang, W. Liu, Y. Feng, X. Rui and Y. Yu, *Mater. Chem. Front.*, 2021, **5**, 3132–3138.
79 F. Li, H. Sheng, H. Ma, Y. Qi, M. Shao, J. Yuan, W. Li and W. Lan, *ACS Appl. Energy Mater.*, 2023, **6**, 6201–6213.
80 S. Deng, H. Li, B. Chen, Z. Xu, Y. Jiang, C. Li, W. Xiao and X. Yan, *Chem. Eng. J.*, 2023, **452**, 139115.
81 Y. Liu and X. Wu, *Nano Energy*, 2021, **86**, 106124.
82 X. Zhao, L. Mao, Q. Cheng, F. Liao, G. Yang and L. Chen, *Carbon*, 2022, **186**, 160–170.
83 X. Chen, X. Hu, Y. Chen, X. Cao, Y. Huang, H. Zhang, J. Liu, Y. Wang, S. Chou and D. Cao, *J. Mater. Chem. A*, 2022, **10**, 22194–22204.
84 X. Yuan, Y. Nie, T. Zou, C. Deng, Y. Zhang, Z. Wang, J. Wang, C. Zhang and E. Ye, *ACS Appl. Energy Mater.*, 2022, **5**, 13692–13701.
85 Y. Qi, X. Jin, L. Xu, X. Ren, Y. Xia and J. Alloy, *Compounds*, 2023, **967**, 171750.
86 Z. Song, Y. Zhao, H. Wang, A. Zhou, X. Jin, Y. Huang, L. Li, F. Wu and R. Chen, *Energy Environ. Sci.*, 2024, **17**, 6666–6675.

87 D. Zhang, J. Cao, X. Zhang, J. Qin and Z. Zeng, *ACS Appl. Mater. Interfaces*, 2023, **15**, 57230–57238.
88 X. Gu, J. Wang, S. Wu, S. Dong, F. Li, A. Cui, M. Zhang, P. Dai and M. Wu, *Mater. Adv.*, 2023, **4**, 5206–5214.
89 Z. Luo, J. Zeng, Z. Liu, H. He and J. Alloy, *Compounds*, 2022, **906**, 164388.
90 J. Guo, L. Li, J. Luo, W. Gong, R. Pan, B. He, S. Xu, M. Liu, Y. Wang and B. Zhang, *Adv. Energy Mater.*, 2022, **12**, 2201481.
91 L. Ma, X. Wang, X. Chen, J. Gao, Y. Wang, Y. Song, Y. Zhao, S. Gao, L. Li and J. Sun, *Nano Res.*, 2024, **17**, 7136–7143.
92 Y. Li, X. Liao, B. Xie, Y. Li, Q. Zheng and D. Lin, *J. Colloid Interface Sci.*, 2024, **662**, 404–412.
93 J. S. Park, J. H. Jo, Y. Aniskevich, A. Bakavets, G. Ragoisha, E. Streltsov, J. Kim and S. T. Myung, *Chem. Mater.*, 2018, **30**, 6777–6787.
94 B. B. Deka, A. Mathieson, S. K. Park, X. Zhang, B. Wen, L. Tan, A. Boies and M. De Volder, *Adv. Energy Mater.*, 2021, **11**, 2100115.
95 J. H. Choi, J. S. Park and Y. C. Kang, *Appl. Surf. Sci.*, 2022, **599**, 153890.
96 J. Li, J. Zhao, Z. Wang, H. Liu, Q. Wen, J. Yin and G. Wang, *Materials*, 2024, **17**, 2817.
97 D. Zhao, Z. Li, D. Xu and Z. Yang, *Adv. Funct. Mater.*, 2024, **34**, 2316182.
98 Y. Jin, X. Zhang, Y. Zhu, J. Ye, Y. Qian and Z. Hou, *ACS Appl. Mater. Interfaces*, 2024, **16**, 28391–28401.
99 H. Geng, T. Zhou, H. Cao, Y. Li and J. Wang, *J. Energy Storage*, 2024, **91**, 111985.
100 J. Guo, J. Ming, Y. Lei, W. Zhang, C. Xia, Y. Cui and H. N. Alshareef, *ACS Energy Lett.*, 2019, **4**, 2776–2781.
101 B. D. Boruah and M. D. Volder, *J. Mater. Chem. A*, 2021, **9**, 23199–23205.
102 B. Shuai, C. Zhou, Y. Pi and X. Xu, *ACS Appl. Energy Mater.*, 2022, **5**, 6139–6145.
103 H. Hu, P. Zhao, X. Li, J. Liu, H. Liu, B. Sun, K. Pan, K. Song and H. Cheng, *J. Colloid Interface Sci.*, 2024, **665**, 564–572.
104 Z. Li, Y. Ren, L. Mo, C. Liu, K. Hsu, Y. Ding, X. Zhang, X. Li, L. Hu, D. Ji and G. Cao, *ACS Nano*, 2020, **14**, 5581–5589.
105 R. Li, L. Wang, Y. Tian, Y. Chao, X. Cui and Q. Xu, *Mater. Lett.*, 2023, **346**, 134541.
106 Z. Yuan, F. Xiao, Y. Fang, P. Xiong, X. Sun, X. Duan, X. Yang, H. Fan, M. Wei, Q. Qian, Q. Chen and L. Zeng, *J. Power Sources*, 2023, **559**, 232688.
107 R. Si, S. Yi, H. Liu, F. Yu, W. Bao, C. Guo and J. Li, *Chemistry*, 2023, **29**, e202300409.
108 S. Huang, S. He, H. Qin and X. Hou, *ACS Appl. Mater. Interfaces*, 2021, **13**, 44379–44388.
109 X. Liu, Z. Xu, J. Wu, K. Wang and C. Yu, *J. Colloid Interface Sci.*, 2025, **678**, 35–44.
110 X. Gu, J. Wang, X. Zhao, X. Jin, Y. Jiang, P. Dai, N. Wang, Z. Bai, M. Zhang and M. Wu, *J. Energy Chem.*, 2023, **85**, 30–38.
111 F. Gao, H. Gao, K. Zhao, X. Cao, J. Ding and S. Wang, *J. Colloid Interface Sci.*, 2023, **629**, 928–936.
112 M. Li, J. Mou, L. Zhong, T. Liu, Y. Xu, W. Pan, J. Huang, G. Wang and M. Liu, *ACS Sustainable Chem. Eng.*, 2021, **9**, 14193–14201.
113 S. Wang, H. Zhang, K. Zhao, W. Liu, N. Luo, J. Zhao, S. Wu, J. Ding, S. Fang and F. Cheng, *Carbon Energy*, 2023, **5**, e330.